DEGREE PROJECT

L

Microstructure and Mechanical Investigation of Carbides Particles Reinforced High Austenitic Manganese Steel

Abderrahim Ait Ouakrim

LULEÅ
UNIVERSITY
OF TECHNOLOGY
L

ABSTRACT

The objective of this study was to produce a metal matrix composite (MMC). This composite material proves highly suitable for scenarios involving abrasive wear, owing to the exceptional hardness of carbide particles, in conjunction with the remarkable ductility and capacity for work hardening found in Hadfield steel. Therefore, the effect of WC and TiC on the microstructure, mechanical properties, and wear resistance was investigated. The X-Ray Diffraction (XRD) technique and Scanning Electron Microscope coupled with Energy X-ray Dispersive Spectroscopy (SEM-EDS) were employed to examine the phase transformation and microstructure characteristics of the MMCs. The grain size of carbides was calculated using ImageJ software. The wear test was conducted using a mini jaw crusher equipped with a stationary jaw (SJ) and movable jaw (MJ). The wear characterization involved assessing volume loss, hardness profile, and the worn surface. The microstructures showed the formation of carbides particles dispersed within the matrix. Compared to the hardness of the manganese steel matrix, the MMCs exhibited a significant increase in hardness. Regarding the wear performances, the movable jaw (MJ) demonstrated greater resistance (lower volume loss) compared to the stationnary jaw (SJ), indicating different wear mechanisms between the two jaws. The worn surface exhibited a textured appearance with visible grooves, scratches, and embedded abrasive fragments. The hardness profile from the worn surface towards the core displayed a gradual decrease for both the SJ and MJ, indicating the work hardening capacity of manganese steel

Key words: **Metal Matrix Composites (MMCs), Manganese steel, Carbides particles, Wear resistance.**

ACKNOWLEDGEMENTS

Contents

List of Figures

List of Tables

Chapter 1

General introduction

Crushing rocks is the main process of mining industries. Several crushing processes can be distinguished (primary, secondary, tertiary ...), generally depending on the size of raw materials. Moreover, several crushers such as jaw, impact, gyratory, cone, etc. can carry out crushing operations. Cone crusher shown in **Figure 1.1** is widely used in mining, it consists of two main parts: the mantel (Movable part) and the concave (Stationary part). The mantle is moving in an eccentric motion, which means that it does not remain completely centered, but swings slightly as it rotates, continually altering the gap between it and the concave. Therefore, as the mantle moves, it crushes the material against the concave at the points where the gap is smallest. The Closed Side Setting (CSS) is a very important parameter since it defines the maximum product size and has significant bearing on crusher's performances [1].
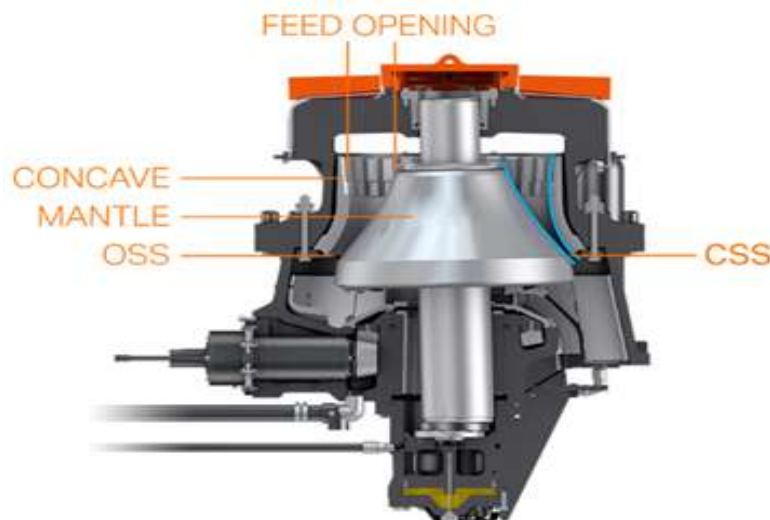
Figure 1.1: Operating principle of cone crushers.

In the last decades, many studies have put the focus on Matrix Metal Composites (MMCs) materials since they combine the best properties of both the matrix and reinforcement. The matrix generally carries the loads and provides stability to the composite structure. Meanwhile, the dispersed phase as ceramics ($WC, TiC, NbC, VC...$) are commonly used to improve mechanical properties such as strength, wear resistance, hardness... etc [2].

High manganese austenitic steel, also called Hadfield steel, is commonly used for rock crushing due to its properties such as high abrasion resistance when compared to other steels,

work-hardening ability along with high levels of ductility and toughness. These unique properties therefore make Hadfield steels suitable candidate materials to produce jaw crushers [3]. The jaws crusher (stationary and movable) need to possess significant hardness for rock crushing while also exhibiting sufficient toughness to withstand the impact energy generated by the movable jaws without experiencing any failures [4]. Despite all these properties, Hadfield steels suffer from low hardness and mass loss (weak wear resistance) due to the friction over time, which leads to premature failure of wear parts during crushing operations and thereby enormous economic and environmental cost to the company [3]. Adding *WC*, *TiC* or their combination can significantly improve the wear resistance and hardness of Hadfield steels as well as their service life during crushing operations. Many studies have been investigated the effect of carbides on mechanical and microstructural properties [3, 5].

It is very well known that by selecting appropriate raw materials, compositions and suitable processing parameters, a wide combination of mechanical properties can be achieved. The focus of this project is to develop a Metal Matrix Composite (MMC) and then to investigate the microstructure, mechanical properties (hardness, impact toughness), and wear resistance. The current study is structured into three main chapters:

- The first chapter provides an overview on the manufacturing routes of MMCs samples.

- The second chapter focuses on the experimental procedure followed throughout the project, including the starting materials, fabrication of inserts, casting and heat treatment, and the techniques used for the microstructural and compositional characterization of specimens. Furthermore, the chapter details the instrumentation employed to measure the mechanical properties such as hardness and wear resistance.

- The last chapter presents the results obtained from the characterization tests and discusses the implications of the findings.

- Finally, the report concludes with a general summary of the study's key findings and future perspectives.

Chapter 2

Literature review

This chapter focuses on five key areas. Firstly, it introduces Metal Matrix Composites (MMCs) and their various fabrication routes. Secondly, it offers an overview of high austenitic manganese steels, also known as Hadfield steels. The third area discusses tungsten carbide and titanium carbide, as well as their combination, as reinforced phases within the Hadfield steel matrix.

2.1 Introduction & fabrication routes of MMCs

Matrix Metal Composite (MMC) is a composite material with at least two constituent parts: one being a metal called matrix, the other might be a ceramic or an organic compound. On one hand, the matrix plays an important role as it provides support for the dispersed phase (carry the loads, provide stability to the composite structure). On the other hand, the reinforcement is used to improve mechanical properties such as strength, wear resistance, hardness... etc [2]. MMCs are commonly classified according to the nature of reinforcement. Three categories of reinforcement can be distinguished: **(i):** continuous or long fiber, **(ii):** discontinuous or short fiber and **(iii):** reinforcement in the form of particles, see **Figure 2.1 [6]**.
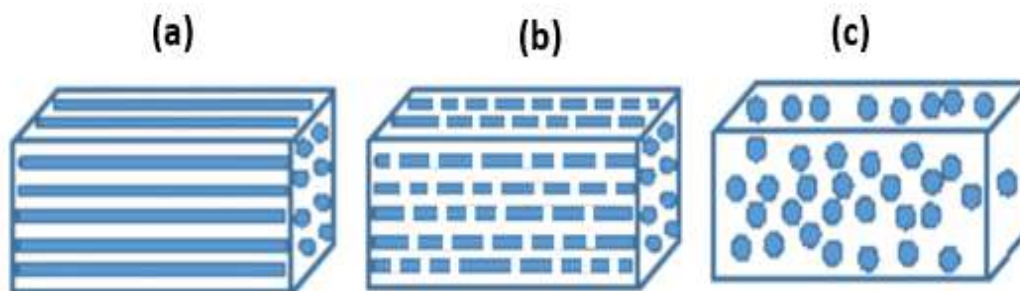
Figure 2.1: Schematic of different types of reinforcement, (a): Continuous fibers, (b): Discontinuous fibers, and (c): Particles reinforced [6].

In the present work, the matrix is Hadfield steel, and the reinforcement is carbides particles (WC and TiC). These carbides can be precipitated inside the austenitic grains as well as at grain boundaries, especially in parts with a thick cross section [7]. A schematic of the microstructure of Hadfield steels is shown in **Figure 2.2**.
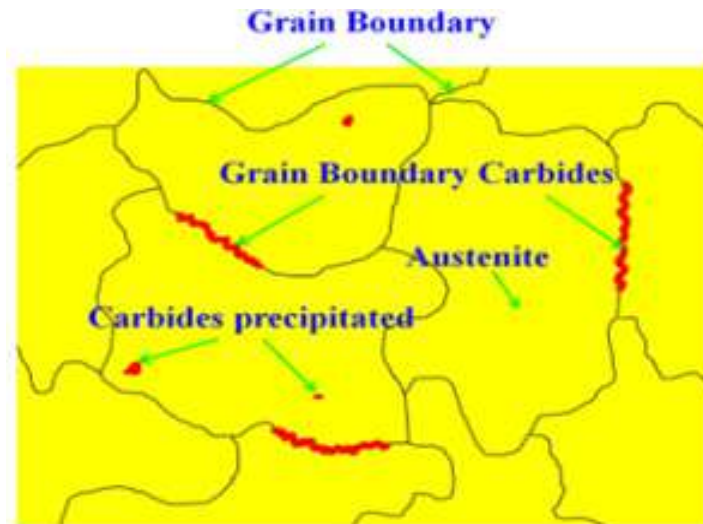
Figure 2.2: A schematic of the microstructure of Hadfield steels [7] .

Several production routes are used to fabricate MMCs. Moreover, each route leads to different characteristic composites despite of the same composition and contents of the constituents. The classification of manufacturing methods for Metal Matrix Composites as seen in **Figure 2.3** can be categorized into several processes based on which how the reinforcement materials are incorporated into the metal matrix. Here are the primary classification categories:
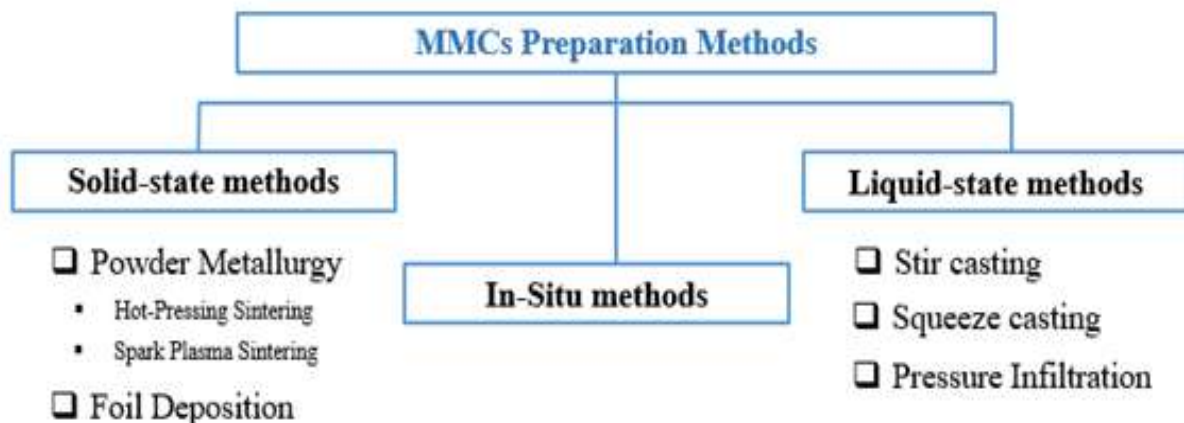
Figure 2.3: Classification of manufacturing methods of MMCs [8] .

2.1.1   Solid-state methods

Solid-state processes use high temperature and pressure to generate atomic diffusion between the metal matrix and the dispersed phase [2]. For example, Spark Plasma Sintering (SPS) (**Figure 2.4-a**) involves the consolidation of powders using pressure assisted with pulsed direct electric current, Hot-Pressing Sintering (HPS) (**Figure 2.4-b**) is based on applying high pressure and temperature at the same time [9]. Moreover, foil deposition method (**Figure 2.4-c**) in which multilayers of different metals are arranged and compacted into a single composite with reinforced long fibers.…etc [8]. Solid-state processes are generally used to obtain higher mechanical properties.
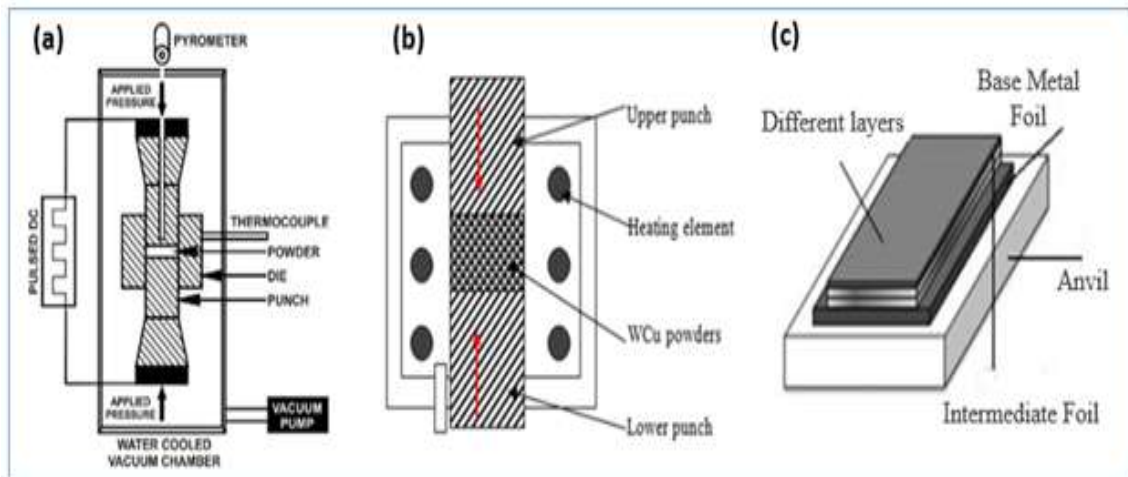
Figure 2.4: Solid-state methods: (a): Spark plasma sintering, (b): Hot pressing sintering and (c): Foil deposition [8, 9].

2.1.2 Liquide-state methods

In these methods, the dispersed phase is incorporated into a metal matrix at its molten state. These processes are characterized by strong interfacial bonding and are relatively simple and cost effective compared to solid state processes [2]. Liquid state processes include stir casting and infiltration methods, they are widely used for preparing MMCs [10].

In stir casting method (**Figure 2.5-a**), the reinforcing phase is mixed with the metal matrix through mechanical stirring. The metal matrix or alloy is first melt, and then the reinforcement particulates or fibers are added. A stirrer is used for both stirring and uniformly distributing the heat and reinforcement phase [11]. Suresh et al. [12] reinforced aluminum alloy (Al6061) with TiB_2 particles by stir casting method. The inclusion of reinforcement TiB_2 improved the mechanical properties and wear resistance of the matrix.

Regarding infiltration methods, tree types of processes can be distinguished [11]:

- **Gas Pressure Infiltration:** this method is performed using a gas for applying pressure on the molten metal and forging it to penetrate a preformed dispersed phase [13]. This process is shown in **Figure 2.5-b**. Compared with the processes using mechanical force, Gas Pressure Infiltration process does not much destroy and damage the fibers [11]. Moreover, it allows manufacturing composites with high compaction and infiltration.

- **Squeeze Casting Infiltration:** this method consists of applying a ram force to the molten metal. The upper die, which is movable, moves downward and forces the liquid metal to infiltrate a preformed dispersed phase as shown in **Figure 2.5-c**. This method generates less pores due to the high pressure at which the process is carried out [10, 12].

- **Pressure die infiltration:** Die-casting consists of forcing a metal in its molten state into a die with help of a movable piston. The preformed reinforcement phase is placed in the die and the molten metal is infused with the preform, which results in a uniform MMC. This process is shown in **Figure 2.5-d**. One of the challenges of this technology is that the

preform can displace due to very high-pressure, which affects the quality of products [11].
.
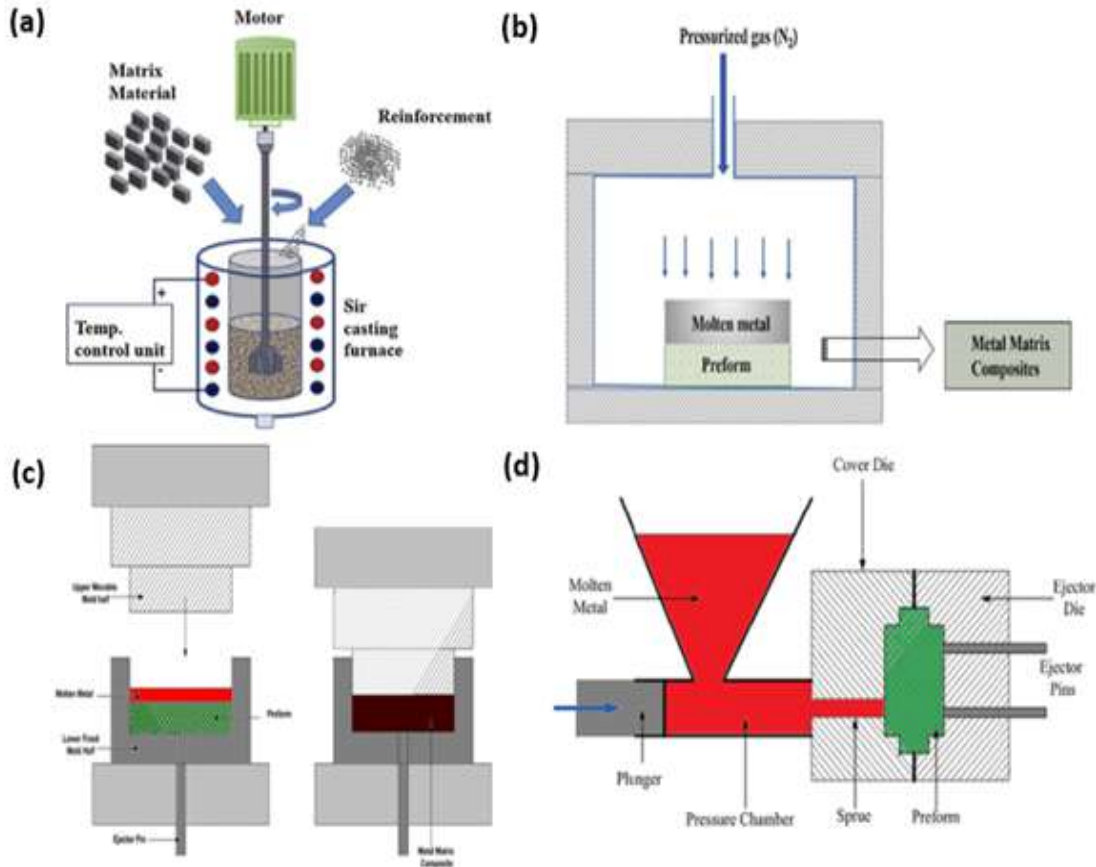
Figure 2.5: Liquide-state processes: (a): Stir Casting method, (b): Squeeze Casting Infiltration, (c): Gas Pressure Infiltration, (d): Pressure Die Infiltration [11, 13].

2.1.3 In-Situ methods

Besides solid-state and liquid-state methods, in-situ methods are based on producing the reinforcement during the process itself. In other words, the dispersed phase results from the precipitation or nucleation generally via chemical reaction. in-situ methods offer the advantage of having better distribution of the reinforcement in the matrix phase, as well as having less impurities at the interface (the reinforcement surfaces are likely to be free of contamination), which results in good bonding. Moreover, equipment used for an in-situ manufacturing of Metal Matrix Composites are less expensive [13]. Overall, in-situ fabrication methods of composites provide opportunities to tailor the composition, microstructure, and properties of MMCs, resulting in enhanced mechanical, thermal, and wear resistance characteristics compared to conventional composite manufacturing methods.

2.2 Matrix: Hadfield steels

Hadfield steels also called austenitic manganese steels are non-magnetic alloys, produced mainly by casting [14], and made up of iron (Fe), 1 - 1.4 wt% of carbon and 10 - 14 wt%

of manganese (C-to-Mn ratio of 1:10). Besides, they contain also other elements such as chromium (Cr), silicon (Si), nickel (Ni) ... etc [7]. In 1882, Robert Hadfield produced the first austenitic manganese steel, containing about 1.2 and 12 wt% of carbon and manganese, respectively. Hadfield steels have been widely used in several engineering applications such as mining, quarrying, earthmoving, railways and construction industries [15]. They have unique resistance to abrasion wear as well as high levels of ductility and toughness. Moreover, Hadfield steels possess slow crack propagation rates [3].

Manganese (Mn) is the most important austenite stabilizer in Hadfield steel. Its role is to delay the austenite to martensite transformation (reducing the temperature of martensite transformation) [16]. Moreover, it reacts with carbon and forms carbides (Mn_3C and $(Fe, Mn)_3C$) [3, 13]. The presence of high proportion of Mn gives Hadfield steels a face center cubic (FCC) structure, increases the wear resistance and affects both, the ultimate tensile strength (UTS) and ductility [16]. Venturelli et al. [14] studied the effect of manganese content (5, 8, 12, 15 and 18 wt%) on the microstructure, impact toughness and wear properties of Hadfield steels (C, Mn, Si, Mo, P and S). The finding results are summarized in Table 2.1. Machado et al. [17] investigated the abrasive wear resistance of Hadfield steel with 12 and 20 wt% Mn via jaw crusher test. They found that the predominant mechanisms of wear between the stationary jaw (Indentations, some scratches) and movable jaw (Cutting and Ploughing) are different. Meanwhile the mass loss or MJ/SJ ratio (mass loss of movable jaw divided by mass loss of stationnary jaw) showed differences of 55% and 32% when the amount of Mn is 12 and 20 wt%, respectively.

Table 2.1: Effect of manganese content on hardness, impact toughness and wear resistance of Hadfield steel [14].

Alloy	Hardness HV (10 kgf)	Charpy energy (J)	Weigth loss (mg)	Comments
5-Mn	218 ± 6	52 ± 5	870 ± 24	• MnS particles were found by EDS analysis.
8-Mn	218 ± 8	120 ± 8	710 ± 18	• Hadfield steel with 15 wt% Mn had the highest values of the toughness (249 J) and hardness (226 HV).
12-Mn	223 ± 4	199 ± 10	790 ± 52	• The increase in charpy impact
15-Mn	226 ± 5	249 ± 21	790 ± 29	energy is associated with a reduction in wear resistance (Case of Hadfield
18-Mn	217 ± 6	225± 22	820 ± 102	steels that contain 8 and 12 wt% of Mn.

2.2.1 Effect of alloy elements

Alloy elements can be categorized into different groups based on their effects on the material's structure and properties. There are γ-stabilizers that enhance the expansion of the γ-phase region and decrease the temperature at which cementite begins to precipitate. On the other hand, α-stabilizers have the opposite effect to γ-stabilizers. There are also elements that tend to form carbides and elements that do not readily form carbides. These elements are listed in Table 2.2.

The effect of alloying elements on the phase transformation in steels during the processing and their influence on mechanical properties can significantly change based on their size and

Table 2.2: Classification of metals reinforced steel during metallurgical processes.

α-stabilizers	γ-stabilizers	carburigen	no carburigen
Cr – Si – Mo	Mn – Ni	Mn – Cr – Mo – W – V – Ti – Nb	Si – Al – Cu – Ni – Co

volume/weight fractions as seen in **Figure 2.6**. Below are some alloys elements that can be added in steels to enhance their properties [16]:

- **Carbon (C):** Hadfield steels have about 1 to 1.4 wt% of C. Carbon enriches the austenite formed during inter-critical annealing leading to an increase in hardenability [18]. The main advantage of having more carbon content is that it increases the abrasive wear resistance, however it decreases tensile strength and ductility [19]. Moreover, carbon may react with other alloying elements and form carbides.

- **Manganese (Mn):** austenitic manganese steels generally contain about 10 to 14 wt% of Mn. The effect of manganese addition has been discussed in detail in **(Section 2)**.

- **Silicon (Si):** The amount of Si in austenitic steels can vary from 1 to 2 wt% and can increase the tensile strength. Generally, the amount of Si does not exceed 1 wt%. When it is above 2.2 wt%, tensile strength decreases. However, when it is lower than 0.1 wt%, the molding process deteriorates [19].

- **Nickel (Ni):** the addition of nickel in the range of 2 - 4 wt%, has a stabilizing effect on the austenite, as it remains in solid solution. Besides, the formation of carbide layers is prevented for a temperature range of 300 to 500 °C and the ductility is increased, while the yield strength is slightly reduced. The wear resistance also decreases when nickel is added [19].

- **Molybdenum (Mo):** it is added in proportions between 0.5 and 2 wt% to improve toughness, reduce cracking and increase yield strength.

- **Chromium (Cr):** The amount of Cr in austenitic manganese steels can vary from 1.5 to 2.5 wt% 14. Because of low cost of chromium addition, it is more commonly used than molybdenum. Chromium carbides, which are not removed by normal heating (up to 1050 °C) can significantly increase the wear resistance.

- **Vanadium (V), Niobium (Nb), Titanium (Ti) and Tungsten (W):** combined with Carbon (C), they can form very hard and wear-resistant carbide compounds (e.g., V_4C_3, VC, TiC, NbC, WC....), which are very effective to provide precipitation hardening in dual phase steels and are beneficial to improve mechanical properties such as hardness, wear and abrasion resistance [12, 14].

2.2.2   Main strengthening mechanisms of steels

Several mechanisms are generally responsible for increasing the strength, and toughness of many alloys. These mechanisms involve mainly grain refinement, solid solution, Orowan
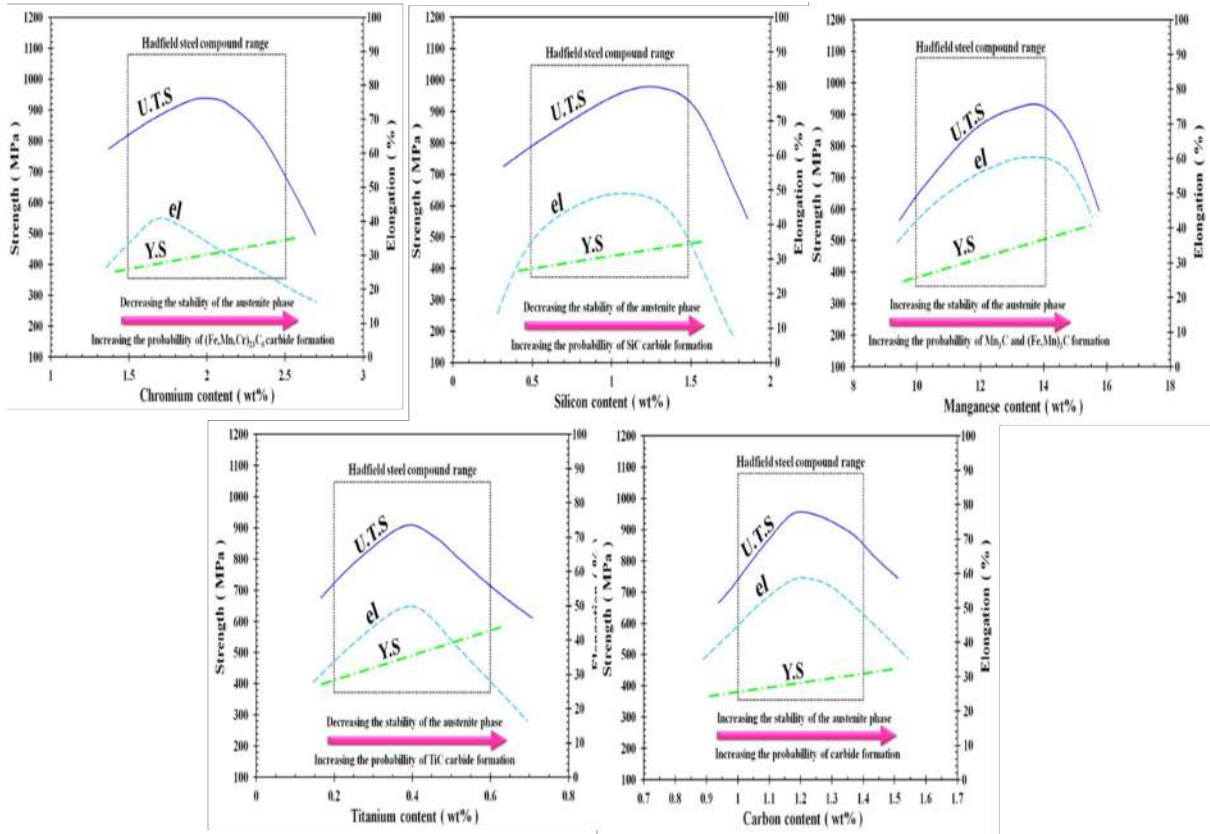
Figure 2.6: A schematic of the effect of alloy elements content on mechanical properties of manganese steel [7].

strengthening, work hardening and heat treatments. Paragraphs below explained briefly theses strengthening methods.

On one hand, a coarse-grained material is less strong and hard than a fine-grained material. This later one has a greater grain boundary area, which forms a barrier for dislocation movement. For many materials, the relation between the grain size and yield strength is given by equation 1 known by Hall-Petch formula [20]:

$$\sigma_y = \sigma_0 + k_y * \frac{1}{\sqrt{d}} \quad \textbf{(1)}$$

Where:

- (d) is the average grain diameter.
- σ_0 and k_y are constants for a particular material.

On the other hand, due to impurity atoms, alloys are usually harder and stronger than metals of the same base metal. These atoms go into either substitutional or interstitial solid solution, impose lattice strains on the surrounding host atoms and restrict the movement of dislocation. Increasing the amount of the impurity results in a significant increase in tensile and yield strengths [17, 20].

Furthermore, strengthening by plastic deformation also called strain hardening or work hardening is often used to harden and strengthen materials that are ductile [20]. For example, during cold rolling or cold forging, the density of dislocation increases, thus the movement of dislocation is impeded by the presence of other dislocations [22]. Equation 2 below defines the degree of plastic deformation as percent cold working (% CW):

9

$$CW(\%) = 1 - \frac{A_d}{A_0} \quad \textbf{(2)}$$

Where:

- A_0 is the area of cross section before plastic deformation.
- A_d is the area of cross section after plastic deformation.

2.2.3 Heat treatments

Heat treatment of steels is an industrial process that modifies the physical, mechanical and/or chemical properties of steels. Heat treating methods include annealing, hardening, quenching, and stress relieving, each method has its own unique process. Moreover, each process consists generally of three main stages: heating stage, soaking/holding stage, and cooling stage.

The heating stage of Hadfield steel ensures the dissolution of alloying elements. The heating rate $(C.min^{-1})$ is an important parameter that must be controlled during heating stage. The austenization temperature, which is generally in the range of 900 - 1150 °C for Hadfield steels affect the microstructure and mechanical properties of steels. Jafarian et al. [23] investigated the effect of austenization temperature on microstructural and mechanical properties of high manganese austenitic steels. The steels have been austenized at 1000, 1075, 1150 and 1225°C, held for 1h and then quenched in water. Results showed that increasing austenization temperature reduced the content of carbides, increased austenite grain size as well as yield/tensile strengths, hardness, and wear resistance of these steels. However, the ductility decreased with increasing the austenization temperature.

During the holding stage, the steel is held for a period also called soaking period until the desired internal structural changes take place. The main objective of holding stage is to ensure the uniformity of temperature throughout the entire volume of steel. Aribo et al. [24] investigated the effect of precipitates on the microstructure and hardness of austenitic manganese steel. They compared two samples aged at 600°C and 700°C for 1, 2, and 3hours. The results showed that the sample aged at 700°C for 2h was found to have finely dispersed carbide particles which results in an increase in hardness.

Regarding the cooling stage, hated materials are often cooled down in oil, air or water.... depending on the material and desired qualities. Lower cooling rate enhances the formability (ductility) of materials and results in bigger grain size. However, quenching in water reduces the grain size and increases the dissolution of carbides [25].

For a given chemical composition of steel, two types of diagrams can be used to better understand the phase transformations during heat treatments [26]. In other word, how heat treatment parameters (time, temperature, cooling environment...) affect the final microstructure and mechanical properties of steels:

- **Transformation-Time-Temperature (TTT) Diagram:** It gives information about the phase transformation and their kinetics when the material is held isothermally at a temperature upon cooling from the austenite temperature. This diagram is shown in **Figure 2.7-a**.
- **Continuous Cooling Transformation (CCT) Diagram:** Identify the start and end of each phase transformation and the corresponding composition during cooling at an approximately constant cooling rate as shown in **Figure 2.7-b**.
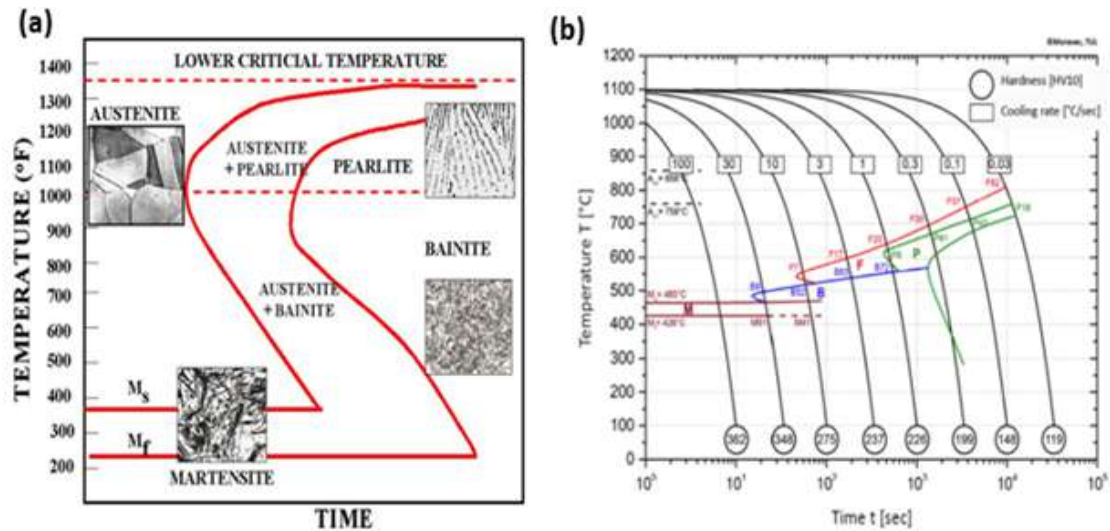
Figure 2.7: (a): The TTT diagram and (b): The CCT diagram of S960MC steel [27].

2.3 Reinforcement

Hard ceramic particles as carbides (ZrC, TiC, W_2C, WC), nitrides (BN, TiN, ZrN), oxides (ZrO_2, Al_2O_3), and borides (TiB_2, ZrB_2, WB) are generally chosen for reinforcing Hadfield steels [28]. One of the most valuable characteristics of theses ceramic particles is their extreme hardness. Thus, they have been widely utilized to enhance the performance of crushing equipment made of Hadfield steels by enhancing the hardness and reducing the mass loss during crushing operations [3, 16]. On one hand, this section presents WC, TiC and $WC - TiC$ system. On the other hand, it discusses the mechanical and microstructural properties of steels when they are reinforced with these sorts of ceramic particles.

2.3.1 Tungsten carbides (WC)

Tungsten carbides are one of the main refractory materials (high melting point over 1800°C), with great prospects in various industrial applications where wear resistance is essential. They are commonly used in the form of cemented carbides (WC particles held by a small amount (5 - 20%) of metallic binder) and their properties depend on the grain size, shape and proportion of carbide to metal [29]. As can be seen in Figure 2.8, the compounds existing in the W–C system are W_2C and WC. W_2C phase crystallizes in several structures (β, β', β'') depending on the carbon content and temperature [30]. Meanwhile WC is the major phase in $W - C$ system. Table 2.3 regroups the main properties of WC at room temperature [29].

Table 2.3: Typical values of properties of WC at room temperature [29].

Structure	Latt. parameters (nm)	Density ($g.cm^{-3}$)	Hardness (GPa)	Melting point (°C)	Young's modulus (GPa)
HPC	a = b = 0.29058 c = 0.28365	15.72	23	2776	707

Moreover, carbon content should be taken into consideration when producing $WC - TiC - Fe$. At low amount of carbon, a sub-stoichiometric carbide phase called Eta-phase (η-phase) can form. This phase has two different carbide forms, namely M_6C, stable at low temperature
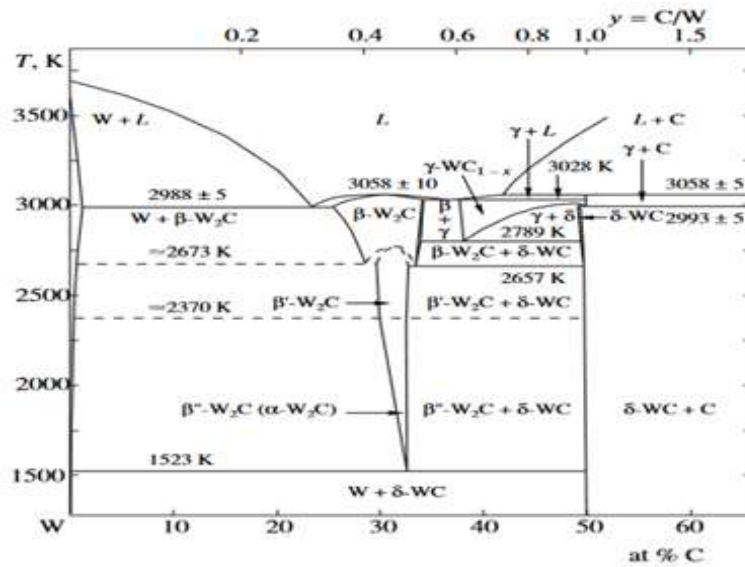
Figure 2.8: W-C binary phase diagram [29].

and $M_{12}C$, stable above 1000 °C. At high amount of carbon, free carbon can precipitate as graphite as can be seen in **Figure 2.9**. Both, Eta-phase and free carbon are undesirable phases that lower the mechanical properties of the material [29].
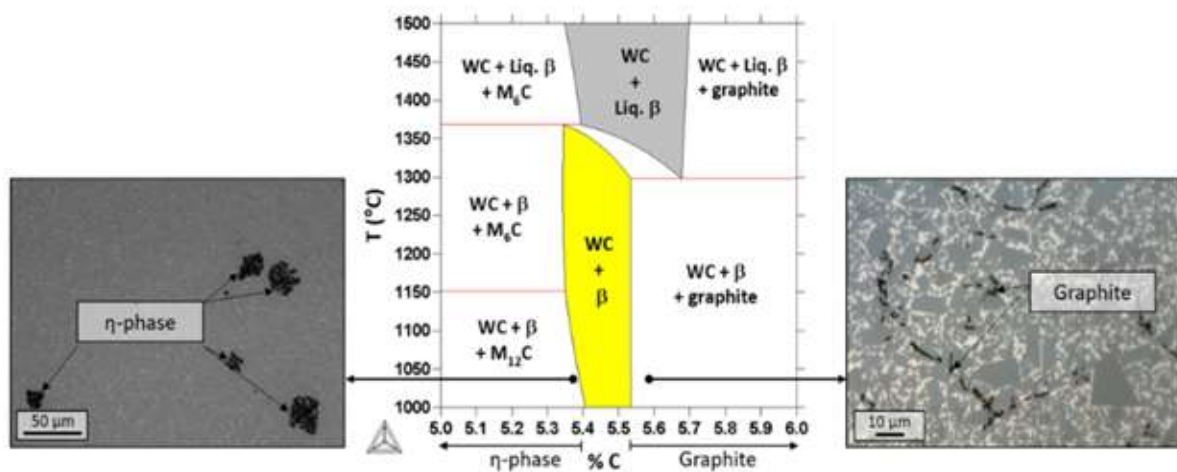
Figure 2.9: η-**phase (left) and graphite (right) formation in a WC-10 wt% Co cemented carbide [29].**

2.3.2 Titanium carbides (TiC)

Titanium Carbide (*TiC*) is an ideal choice for reinforcing steel due to its outstanding attributes. With exceptional hardness, low density, good wettability, and chemical stability with iron, *TiC* offers remarkable advantages. It is widely used as a coating material for cutting tools, thanks to its excellent wear resistance. Additionally, *TiC* demonstrates high resistance to corrosion, making it highly suitable for challenging environments. These exceptional properties make *TiC* invaluable across various industries, especially those that demand materials capable of enduring extreme conditions and demanding applications. **Table 2.4** provides a comprehensive overview of the properties exhibited by *TiC*.

Table 2.4: Typical values of properties of TiC carbides at room temperature [29].

Structure	Latt. parameters (nm)	Density $(g.cm^3)$	Hardness (GPa)	Melting point (°C)	Young's modulus (GPa)
FCC (NaCl)	a = 0.4328	4.91	28	3067	450

Magdaluyo et al. **[15]** found that titanium enhances the hardness and abrasive wear resistance of Hadfield steel through solid solution strengthening and grain refinement. The same results have been reported by Srivastava et al. **[5]**. According to this reference **[29]**, Ti is considered as grain growth inhibitor among other elements such as V, Cr, Ta, Mo and Nb. However, it has been reported that the formation of TiC and carbides generally reduce the formability of the steel **[23]**. Moreover, Srivastava et al. **[31]** investigated the effect of TiC particles on the corrosion of Hadfield steel, they found that increasing the amount of *TiC* increases the corrosion resistance.

Figure 2.10 illustrates the binary phase diagram of the $Ti-C$ system. This system comprises two terminal solids, namely and $\beta - Ti$, along with a refractory monocarbide known as *TiC*. Additionally, the system includes two eutectic reactions and one peritectoid reaction occurring at temperatures of 1646 °C, 2776 °C, and 920 °C, respectively. However, the remaining phases in this system consist of liquid (L) and graphite (C) **[32]**.
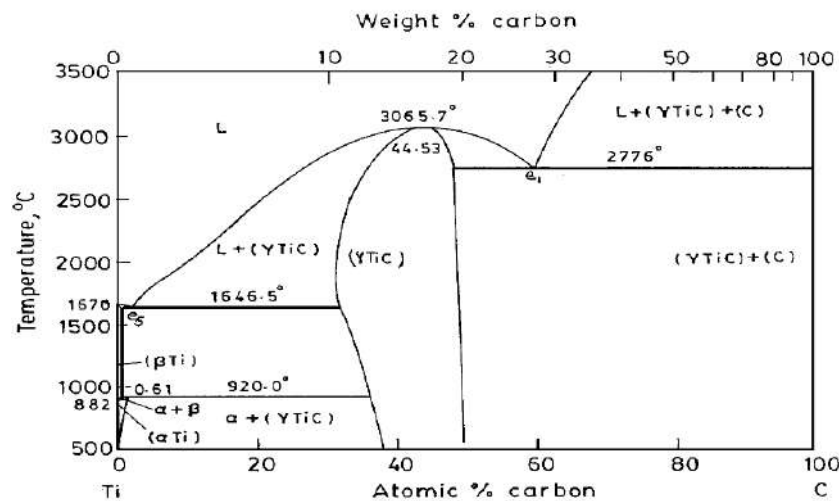
Figure 2.10: Ti-C binary phase diagram [32].

Chapter 3

Materials & experimental procedures

In this chapter, comprehensive information is provided on the starting materials employed in this study, the composition design, and the fabrication of Metal Matrix Composites (MMCs), along with their corresponding heat treatment. Furthermore, the experimental devices employed during the research are detailed, including the equipment and techniques used for sample preparation, microstructural and compositional characterization (SEM, EDS, LOM, XRD), as well as the instrumentation used for measuring the hardness. The compositions that yielded promising preliminary results were further utilized to produce additional samples for wear resistance testing at Sandvik's facilities. A flow chart outlining the experimental procedure followed in this study is presented in **Figure 3.1** , with each step elucidated in detail within this chapter.
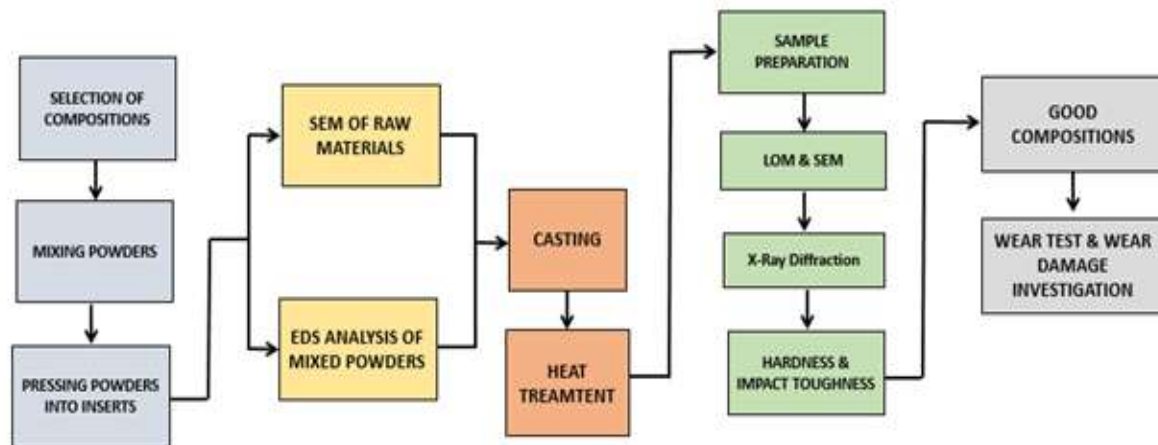
Figure 3.1: Experimental procedure flowchart.

3.1 Fabrication of MMCs

3.1.1 Mixing powders & EDS mapping

The powders have been weighted according to the chosen ratios and introduced into bottles. In these, the powders move freely and easily to ensure homogeneous distribution and thereby

Figure 3.2: The mixing machine.

homogeneous microstructure. Afterwards, the powders were mixed in rotation directions. **Figure 3.2** shows the equipment used for the mixing in which the bottles are put between two metallic rolls driven by an electrical engine.

After the powders were mixed, an EDS analysis was conducted to determine the distribution of each chemical element. The EDS mapping for composition Z4, illustrated in **Figure 3.3**, showed a uniform distribution of powders, indicating successful mixing without any element agglomerations. Furthermore, all elements were visible in the EDS spectrum, and their signals corresponded to the desired composition.
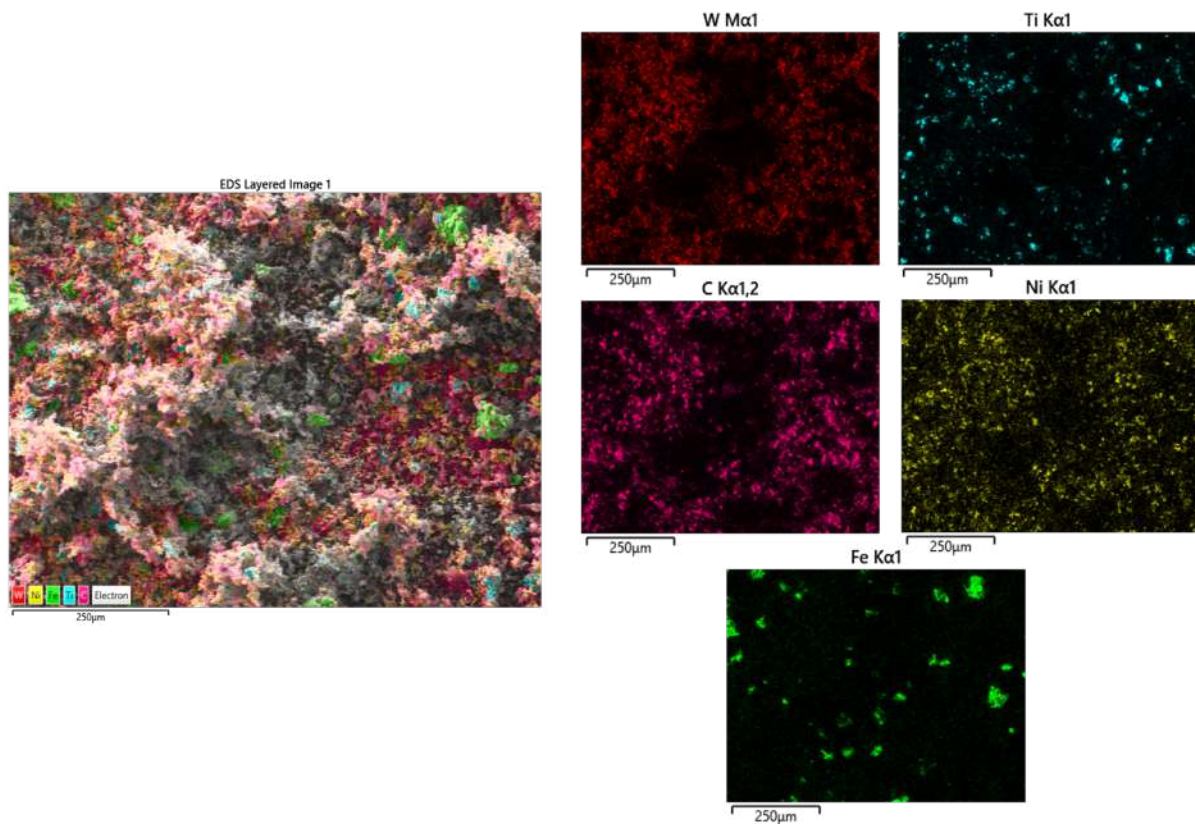
Figure 3.3: EDS result from mixed composition Z4, image mapping left and spectrum right.

3.1.2 Pressing powders into inserts

A hydraulic pressing machine was used to press the mixed powders into inserts. It is shown in figure **Figure 3.4-a** and the pressing steps are summarized in figure **Figure 3.4-b**.
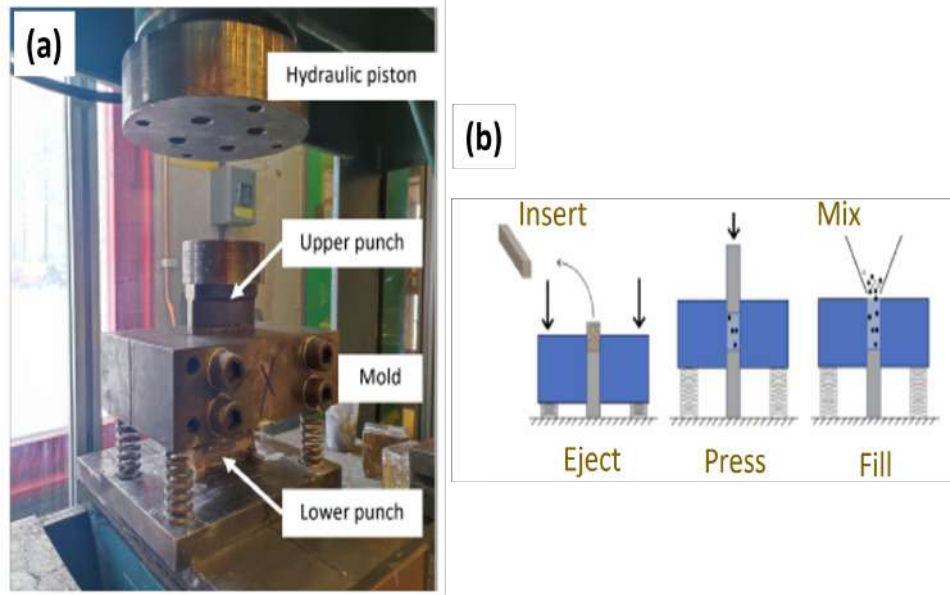
Figure 3.4: (a): Pressing machine configuration and parts, (b): Steps of manufacturing inserts.

1. Initially, the powders were poured in the mold. In fact, when the tungsten mass ratio increases, its amount that should be filled in the mould increases due to its high density.
2. The uniaxial pressing was carried out.
3. Taking out the inserts from the mold was carried out by keeping two blocks on the die and adding pressure until the insert is completely out of the mold.

The pressuring machine used in the study posed several challenges due to its complex design. One of the major issues encountered was the occurrence of lower punch sticking despite the application of lubricant. Additionally, the upper punch sides were observed to be worn out, possibly as a result of previous usage by other students. These factors had a notable impact on the quality of the samples produced. Afterwards, each insert was weighted to calculate its density (ρ_{green}) and then deduced its relative density ρ_0 (%) as well as the porosity that contains using equations **3** and **4** below:

$$\rho_0(\%) = \frac{\rho_{Green}}{\rho_{Theo}} = \frac{\frac{m}{V}}{\frac{1}{\Sigma_{i=1}^{n} \frac{W_i}{\rho_i}}} \qquad \textbf{(3)}$$

$$Porosity(\%) = \frac{\rho_{Theo} - \rho_{Green}}{\rho_{Theo}} = 1 - \rho_0 \quad \textbf{(4)}$$

Where:

- m (g) is the weight of the insert.
- V (cm^3) is the volume of insert.
- ρ_i $(g.cm^{-3})$ is the density of elements that each insert contains.
- W_i (wt%) is the weight fraction.

3.1.3 Casting and heat treatment

For the casting part, the inserts were placed in a sand mold with 8 plates, where each plate contains two inserts. Steel straps have been used to clamp the inserts so they cannot float or move from their positions. Afterwards, the molten Hadfield steel was poured into the mold. The plates were set aside to cool down to room temperature and then separated from the runner and the riser to perform the heat treatment.

After casting, the plates underwent a heat treatment process consisting of several steps: gradual heating, followed by a holding stage at this temperature, and finally quenching in agitated water until reaching room temperature. This heat treatment is a common industrial practice for Hadfield steels [39]. Following heat treatment, it was observed that only the plate corresponding to composition Z2 did not cast properly, and thus show in it was excluded from further characterization as shown in Figure 3.5 . However, all other plates were successful.
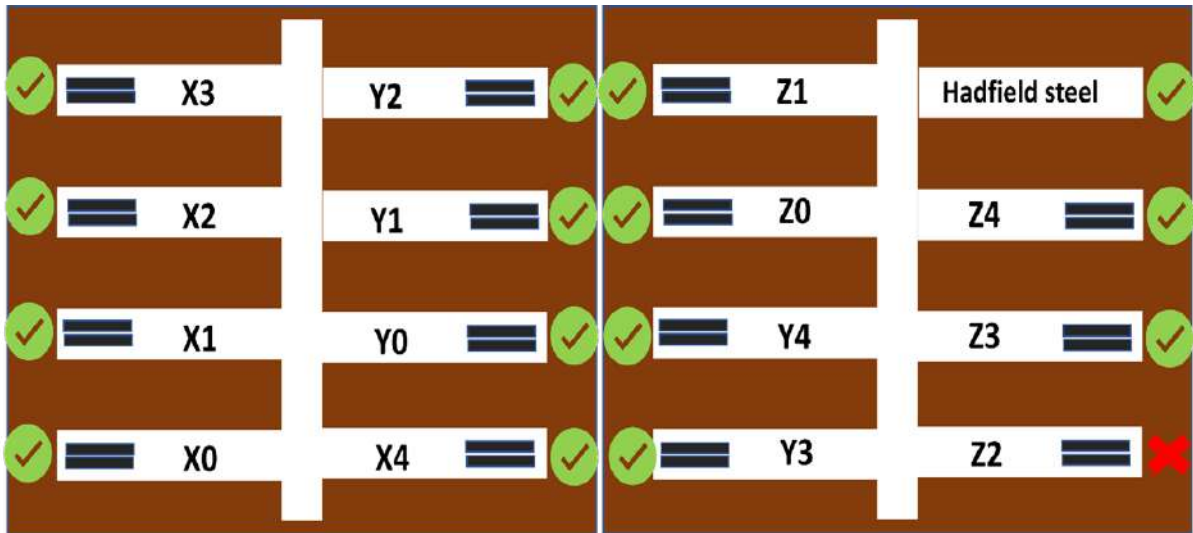
Figure 3.5: Plates distribution after heat treatment: successful and unsuccessful cases.

3.2 Sample preparation

Below are the followed sample preparation steps, they consist of:

Cutting: The plates were cut with Struers Exotom-150 machine using cutting wheels of 50A43 designed for both, Hadfield steel and the reinforced zone. The cutting wheel was running at 2210 rpm and the feed speed was 0.5 $mm.s^{-1}$.

Hot mounting: The hot mounting was performed using a Struers Simplimet 1000 machine and Multifast green resin, which is a conductive thermoset resin. The hot mounting parameters are heating temperature of 180 °C under a force of 20 kN and total time of 10 min.

Polishing: Tergramin-30 semi-automatic polishing machine was performed to get a proper surface for all the sample's characterizations. The polishing steps with their respective polishing cloths, diamond suspension used, time, load, speed, and direction of rotation are listed in Table 3.1 below.

Table 3.1: Procedure of grinding and polishing the samples.

Step	Name	Disc	Lubricant	Time (min)
1	Piano	220	Water	3.5
2	Allegro	All/Lar	Kemet W2	5
3	Dac	Dac	Kemet W2	4
4	Nap	Nap-B	—-	4

3.3 Microstructural characterization

3.3.1 Light Optical Microscopy (LOM)

The utilization of visible light and a collection of lenses in a light optical microscope enables the production of enlarged images of diminutive objects. To capture an overall depiction or macrostructure of the bonding between the matrix and reinforced zone, the Axiocam 105 R2, attached to the Axio Vert.A1 MAT optical microscope, was employed. Furthermore, the samples underwent chemical etching using a 10% Nital solution (10 ml HNO_3 + 98 ml Ethanol) for a duration of 15 seconds to expose the microstructures.

3.3.2 Scanning Electron Microscopy (SEM)

SEM is based on scanning the surface of samples by a focused electron beam. The electron-matter interaction causes different emissions, which are used to form different types of images in a sequential mode. Three types of detectors are placed in the microscope column:

- Secondary electrons (SE) of low energy, are used to form topographic images.
- Backscattered electrons (BSE) of energy close to the excitation energy, are used to form composition images (heavier element will be light).
- X-rays characteristic of the chemical elements present in the sample are analyzed by an energy dispersive spectrometer (EDS).

In this work, morphologies of the starting materials and microstructures of both, manganese steel and Metal Matrix Composites (MMCs) were taken using HITACHI TM 4000 microscope operated at 15 kV and coupled with Aztec software for EDS analysis. Additionally, Image J software was used to measure the average grain size of Hadfield steel and carbides using main linear intercept method.

3.3.3 X-Ray Diffraction (XRD)

XRD is based on irradiating the surface of samples by a monochromatic X-rays beam. Electrons of atoms present in the samples scatter the X-rays beam without changing the wavelength. The incident X-ray beam diffracts in specific directions predicted by Bragg's law as can be seen in equation **5**.

$$\lambda = 2dsin(\theta) \quad \textbf{(5)}$$

Where, λ (nm) and ϑ (°) are the wavelength and the angle of X-ray beam incidence, respectively. d (nm): is the interplanar spacing.

In this work, specimens were characterized by X-ray diffraction (XRD) to analyze the crystalline structures and identify phases that have been formed during casting and heat treatment steps. XRD was conducted using a PANalytical Empyrean, operating at 45 kV and 40 mA with Cu Kα radiation (λ = 0.154 nm) and equipped with Medipix2 detector. XRD measurements were carried out with (2ϑ) in a range 10 – 90° at room temperature with a scan speed of $2.min^{-1}$ and step size of 0.02°. XRD data were analyzed using X'Pert Highscore software and PDF -4+ 2023 (Powder Diffraction File) database.

3.4 Mechanical characterization

3.4.1 Vickers hardness

A standard pyramidal diamond point with a square base and a vertex angle between faces equal to 136°, sufficiently hard not to be deformed, is pressed into the material by the action of a constant applied force.

Vickers micro-hardness (HV) was carried out using Struers Duramin 40. The load was 0.5 kgf with dwelling time of 15 s. For each composition, a total of 18 indentations were made across two lines to measure the hardness profile. Each line had nine indentations: four in the matrix, four in the composite, and one at the interface. The hardness was calculated using equation **6**.

$$Hardness(HV) = 1.8544 * \frac{F}{d^2} \quad \textbf{(6)}$$

Where, F (Kg) is the applied load and d (mm) is the main diagonal length of the indentation.

3.4.2 V-Charpy test

According to GB/T229-2007 national standards of China, the as cast and heat-treated & quenched specimens were machined to 10 mm × 10 mm × 55 mm square cross sections and V-notched (2-mm depth and included angle 45°) (**Figure 3.6**) using an Electrical Discharge Machine (EDM) with the help of the workshop at LTU. Charpy testing was carried out in LTU using JB-30B impact testing machine. The energy absorbed at fracture (E) can be obtained by calculating the difference in potential energy of the pendulum before (h_0) and after (h) the test as shown in equation **7** below. m (g) and g ($m.s^{-2}$) are the pendulum weight and the gravitational acceleration, respectively.

$$E = mg(h_0 - h) \quad \textbf{(7)}$$
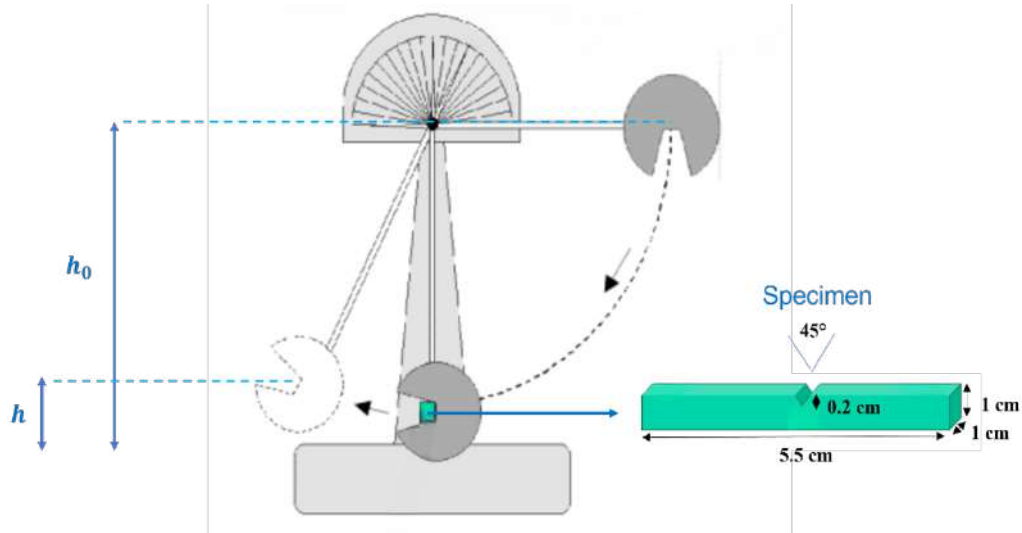
Figure 3.6: Charpy test apparatus.

3.4.3 Wear resistance testing

The ASTM G81-97a (Standard Test Method for Jaw Crusher Gouging Abrasion Test) was employed to conduct the wear testing using a mini jaw crusher (**Figure 3.7**). For each test, two stationary plates and two movable plates were machined and prepared. Subsequently, they were inserted into the machine in such a way that the plates to be tested were positioned in front of the reference plates, which were made of Weldox steel. Weldox steel is renowned for its exceptional wear resistance, and it has been commonly used as a reference material due to its final wear ratio being close to 1. During the test, two tons of rock were crushed, with an interval after one ton. Following each interval, the plates were rinsed with water and then cleaned in an ultrasonic bath to measure their weight loss. The final wear test ratio was calculated using the equation **8**:

$$F = \frac{\frac{X_s}{R_s} + \frac{X_m}{R_m}}{2} \quad \textbf{(8)}$$

Where:

- F = Final wear ratio.
- Xs = Volume loss from stationary test plate(cm^3).
- Xm = Volume loss from movable test plate (cm^3).
- Rs = Volume loss from stationary reference plate (cm^3).
- Rm = Volume loss from movable reference plate (cm^3).
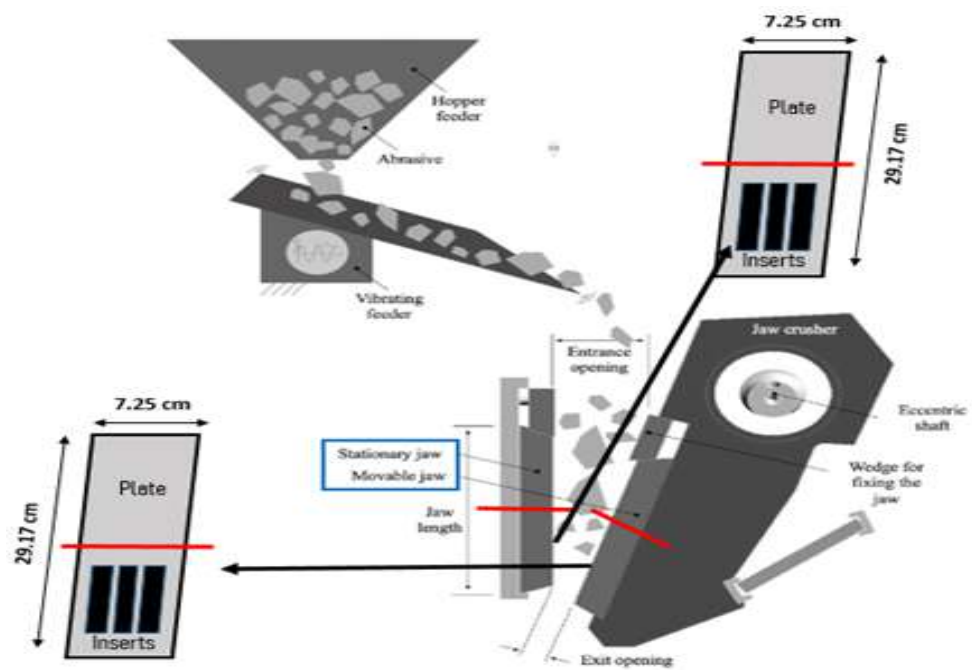
Figure 3.7: Schematic representation of jaw crusher test

Chapter 4

Results & discussions

In this chapter, the focus is to discuss the microstructure, mechanical properties, and wear resistance of Hadfield steels reinforced with WC and $(Ti,W)C$ carbides. The goal is to develop a Metal Matrix Composite (MMC) with improved hardness and wear resistance.

4.1 Green denity of inserts

Figure 4.1 below shows the average relative density of 8 inserts for each composition before casting. It has been calculated as it is considered a valuable parameter for discussing the infiltration of manganese (Mn) during casing.
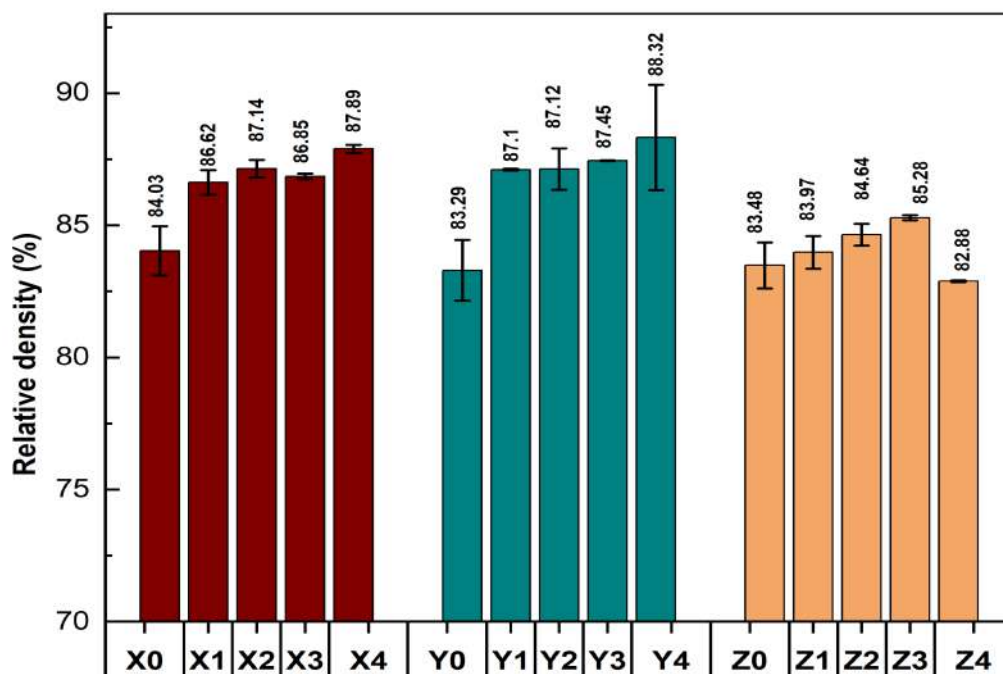
Figure 4.1: Relative density of inserts before casting.

The inserts exhibit a relative density ranging from 82% to 90%. Moreover, it appears that the relative density increases with increasing amount of metallic binder **[54, 55]**, which enhances the compaction and densification. The presence of porosity within the inserts may be attributed

to certain compounds such as H_2O and gases. During casting, these compounds are unable to escape from the sand mold, resulting in their volatilization at high temperatures.

4.2 Macroscopic analysis with LOM

4.2.1 Metal Matrix Composites (MMCs)

Figure 4.2 shows optical micrographs depicting the reinforced zones (gray areas) and the manganese steel matrix (white areas) in categories X, Y, and Z. The micrographs provide clear evidence of the infiltration of manganese steel during the casting process within the reinforced particles composed of $(W, Ti)C$ and WC. However, the micrographs reveal some defects such as pores and cracks either within the matrix or the reinforced zone. The pores are visible, with a more pronounced occurrence in compositions X0 and Y3. The presence of pores is typically attributed to the entrapment of gases, such as hydrogen (H_2), nitrogen (N_2), and oxygen (O_2), within the steel matrix as it solidifies. Furthermore, rapid cooling limits the time available for gases to escape, leading to their entrapment. Additionally, certain alloying elements, such as carbon and sulfur, can increase the likelihood of porosity formation through their reaction with oxygen during solidification $(CO, S_2 \ldots)$. As for the cracks, they are observable in few compositions. Firstly, porosity and inclusions act as stress concentrators, initiating and propagating cracks. Secondly, carbides, being harder and more brittle than the surrounding matrix, are prone to cracking. Moreover, the significant difference in coefficient of thermal expansion (CTE) between the carbides and manganese steel can generate internal or thermal stress during solidification, which can ultimately result in cracking.
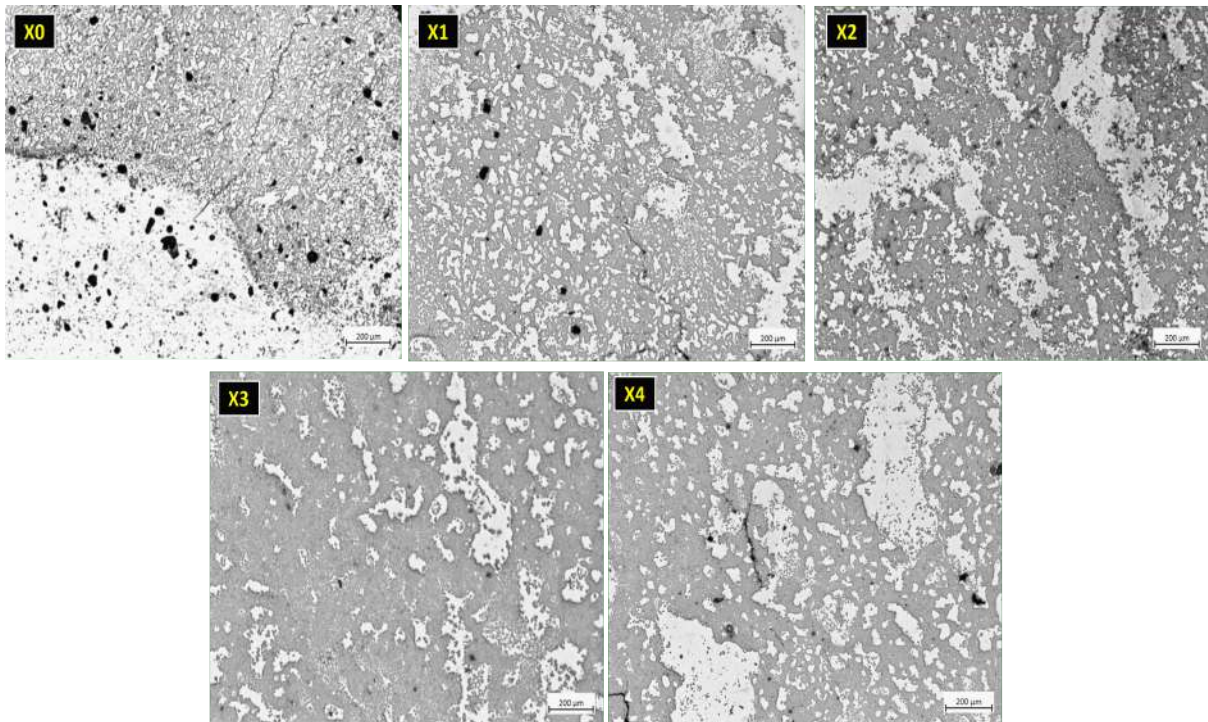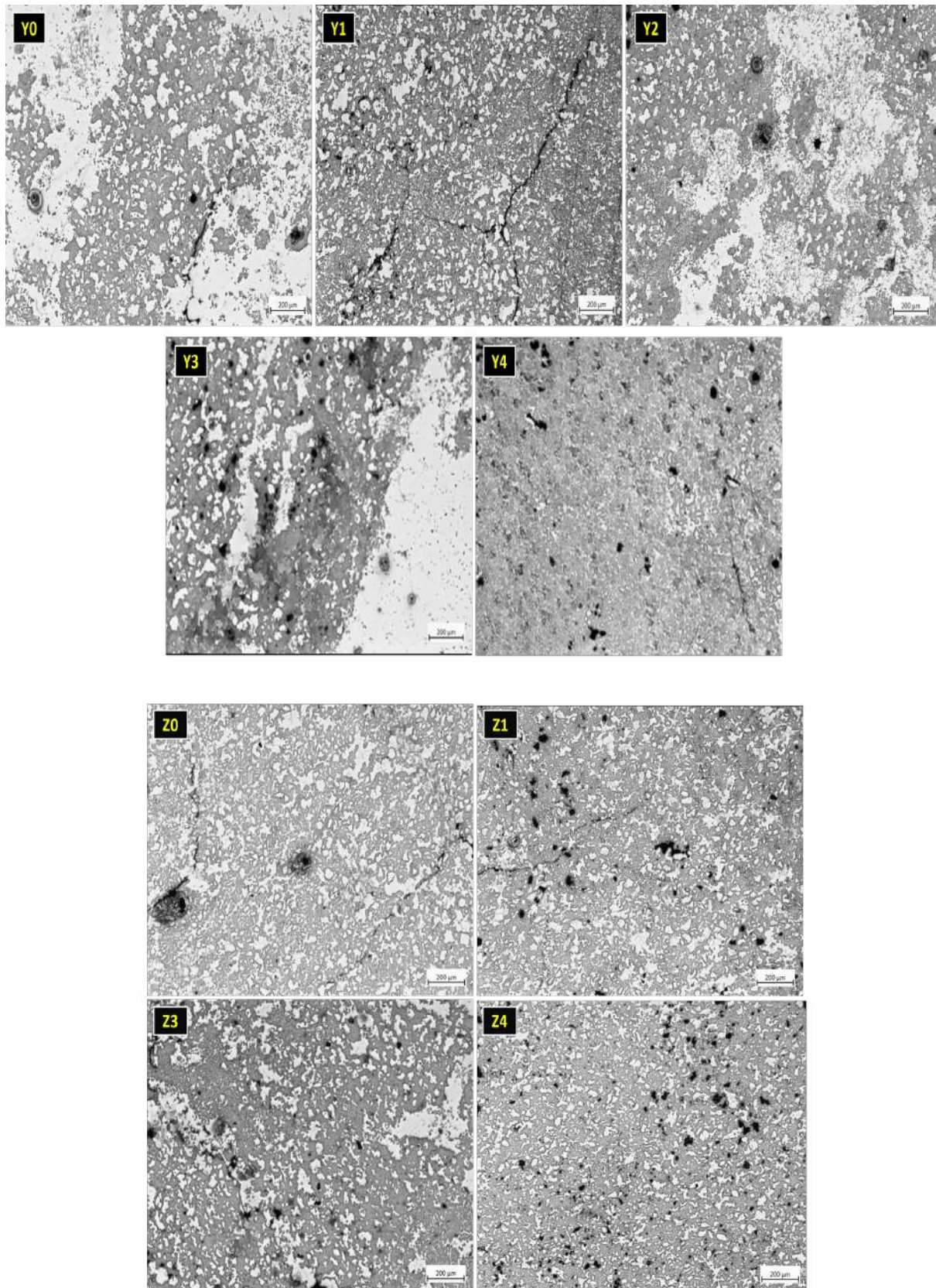
Figure 4.2: Micrographs obtained with LOM of category X, Y, and Z.

4.2.2 Interface Matrix/Reinforcement

The optical micrographs of the interface between manganese steel and the carbides are shown in **Figure 4.3**. Understanding the interface's significance is crucial, as it impacts the mechanical properties of the composite material. A weak interface can lead to stress concentration, resulting in premature failure and reduced overall performance. Conversely, a strong bond facilitates effective load transfer between the matrix and reinforcement. Notably, the optical micrographs confirm good bonding across all compositions. Given that the interface of inserts is more exposed to atmospheric air and initial contact with molten steel, the presence of pores and defects is expected. Moreover, the compositions X2, Z1, and Z4 exhibit a continuous crack at the interface, which can be attributed to the brittleness of carbide particles within the matrix. In composition X1, it can clearly be seen that the crack in the matrix altered its path upon encountering the carbides zone. In other words, carbides can act as crack arrestors, hindering the crack propagation.
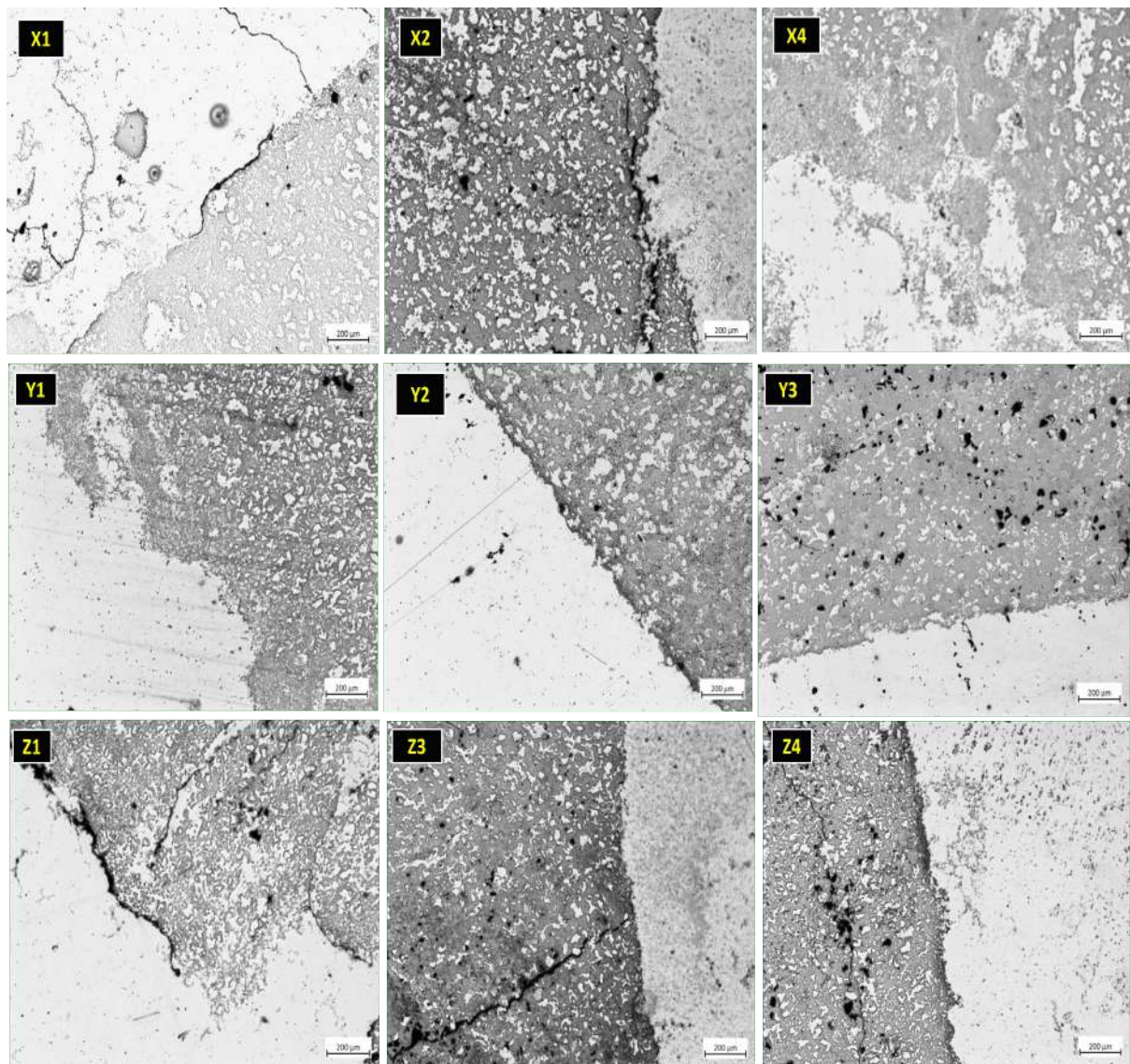
Figure 4.3: LOM Micrographs of the interface in various samples.

4.3 Microstructure characterization

4.3.1 As cast Vs heat-treated & quenched manganese steel

Figure 4.4 presents SEM micrographs of as cast and heat-treated quenched Hadfield steel. The microstructure of the as cast sample shows an austenitic matrix with a continuous carbide phase at the grain boundaries, as evident from the image **(Figure 4.4-(a,b))**. Upon heat treatment, the amount of carbides in the microstructure is observed to decrease, attributed to the quenching process in water, which eliminates the intergranular carbides **[17] (Figure 4.4-(c,d))**.

Based on the analysis of **Figure 4.4-e**, it can be concluded that chromium and manganese are more present at the grain boundaries than within the grain. This observation suggests that the carbides located at the boundaries of the grains consist mostly of chromium and manganese $(Fe, Mn)_3C$ **[5]**. Additionally, the black spots present in the micrographs are porosity generated in the manufacturing process of the Hadfield steel. ImageJ software was utilized for measuring the average particle size using mean linear intercept method detailed in **Annex I**. The as cast sample had an average particle size of 133.2 μm, while the heat-treated and quenched sample exhibited an average particle size of 110.7 μm.
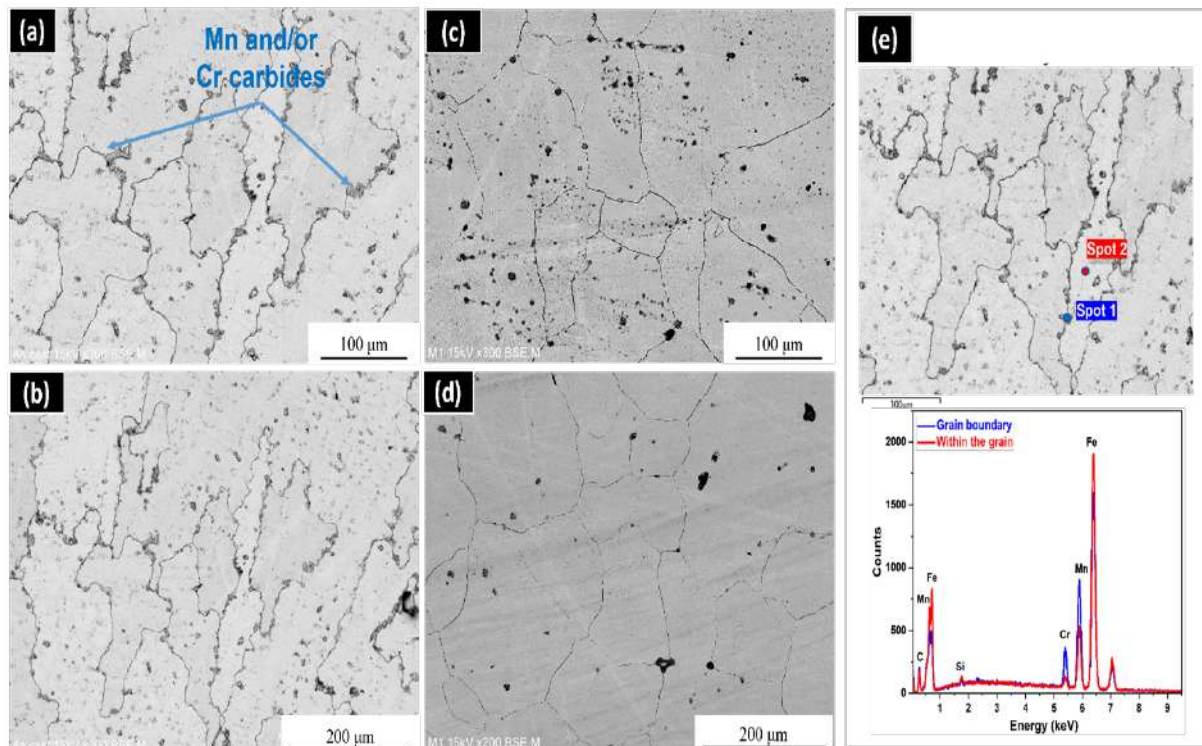
Figure 4.4: SEM micrographs of the Hadfield steel, (a, b): as cast, (c, d): heat treated quenched, (e): EDS spots of as cast steel, spectrum 1: at the grain boundary and spectrum 2: within the grain.

4.3.2 Category X

Figure 4.5 shows the SEM micrographs of compositions X0, X1, X2, X3 and X4. As can be seen in this figure, the microstructure of all these compositions consists only of binary carbides $(W, Ti)C$ also called solid solution or gamma phase (γ-phase). This phase is well known by its

distinct rounded morphology and consists of titanium in the core (black color) surrounded by tungsten (light gray color) presenting a core rim structure [33, 34]. The presence of this phase enhances the strength and as well as the toughness of materials [56].
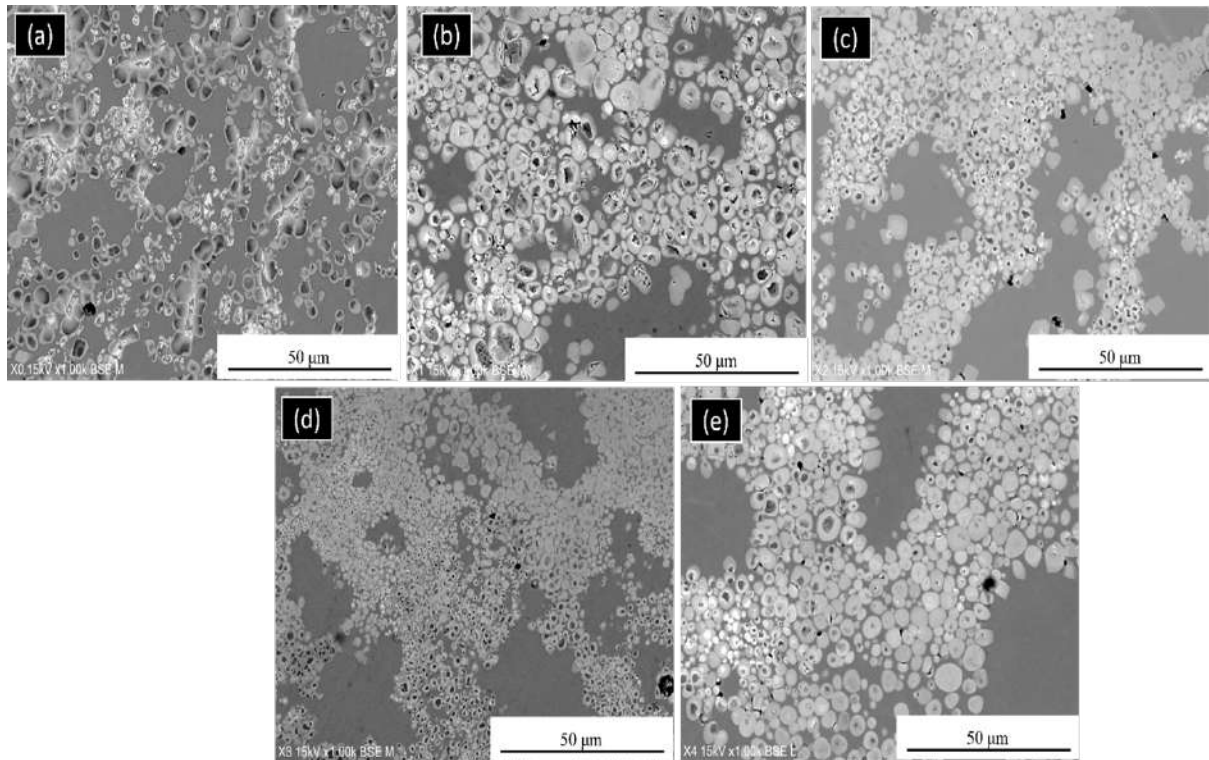
Figure 4.5: SEM images of compositions corresponding to category X, (a): X0, (b): X1, (c): X2 (d): X3 and (e): X4.

Based on the analysis in **Figure 4.6**, it can be seen that the rim phases consist mainly of the $(W, Ti)C$ indicating that the reinforced zone exhibits higher concentrations of tungsten and titanium as shown in X-ray mapping images.

According to the core rim structure, the weight fraction of tungsten should be lower than that of titanium since this latter is present in the inner rim or the core. To investigate this point further, EDS line scanning was conducted across the particulate and the results are shown in **Figure 4.7**. The concentration of titanium increases from the periphery to the core of the gamma-phase particulates whereas the concentration of W decreases, which confirm the morphology of this phase and its mechanism of formation. These findings are consistent with those reported by Srivastava et al. [28].
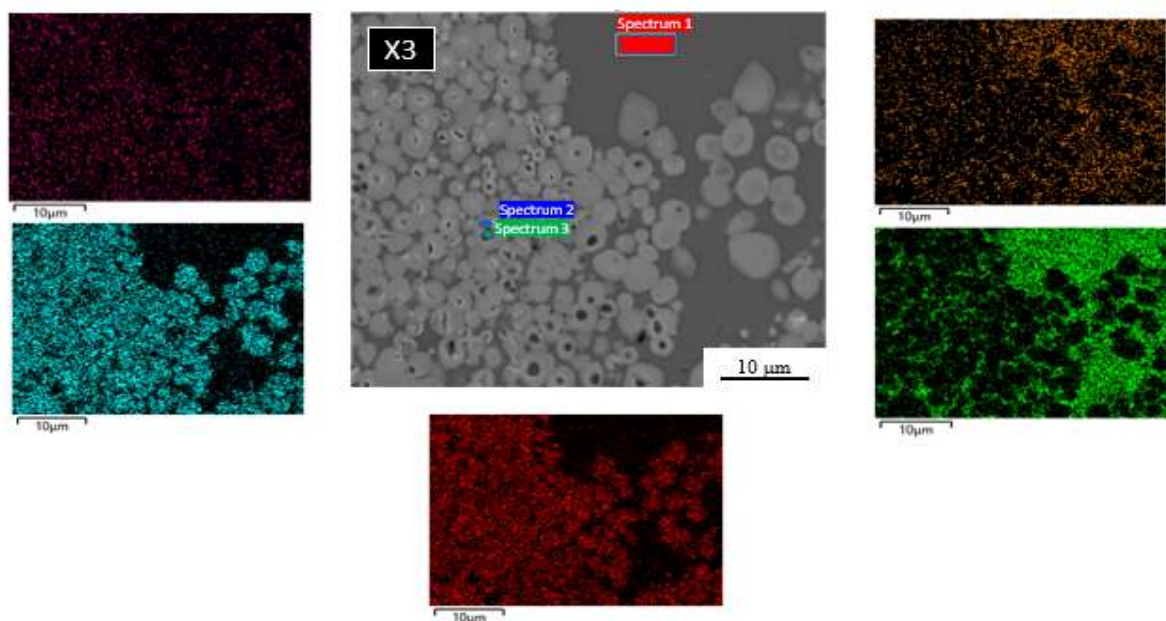
Figure 4.6: EDS spots of composition X3, (a): Matrix, (b): outer rim, (c): inner rim and (d): X-ray mapping results.
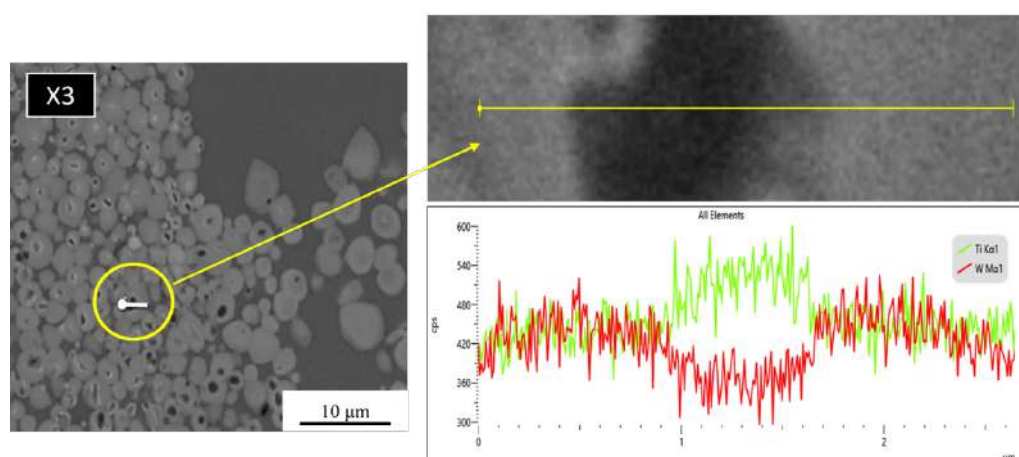
Figure 4.7: EDS linescan across (Ti,W)C particulate.

4.3.3 Category Z

In **Figure 4.8**, SEM micrographs of compositions Z0, Z1, Z3, and Z4 are presented. Their microstructures consist of (WC) grains, $(W,Ti)C$ solid solution (γ-phase), and Hadfield steel matrix. WC-phase appears with white angular shape or prismatic grains. $(W,Ti)C$ solid solution particles appear with rounded morphology, and both are regularly distributed and embedded within the manganese steel matrix represented with dark gray color. $(W,Ti)C$ solid solution is composed of two distinct types of particles. There are small particles, measuring less than 1 μm in size and there are the large particles, which possess a similar size to that of tungsten carbides. The coexistence of different particle sizes within the same phase might be related either to the solidification process or some alloying dopants that alter the growth kinetics [57]. Compared to category X, the presence of WC in compositions Z is due to the higher weight fraction of tungsten, which besides forming $(W,Ti)C$ solid solution, forms also WC. Many Studies have confirmed that iron plays an important role not only in improving the bonding between the matrix and the reinforced zone, but also reducing the particle size of carbides [40, 57]. Moreover, it has been reported that during casting, the thermoplasticity flow of iron (Fe) promotes the rearrangement and distribution of WC particles [55].
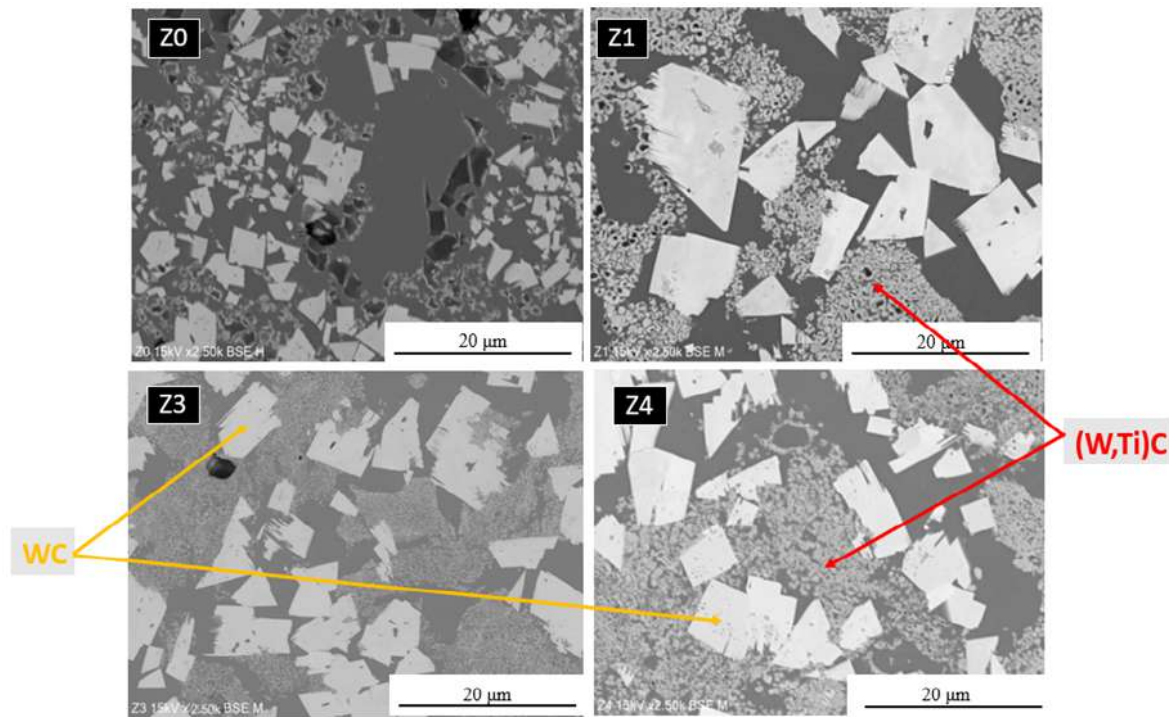
Figure 4.8: SEM images of compositions corresponding to category Z, (a): Z0, (b): Z1, (c): Z3 and (d): Z4.

EDS analysis findings are presented in **Figure 4.9**. They confirm the presence of titanium and tungsten indicating the coexistence of tungsten carbides WC and binary carbides $(W,Ti)C$. These carbide particles are dispersed withing the manganese steel matrix. However, carbon is a likely contaminant in EDS analysis, which makes its weight/volumetric fraction unreliable.
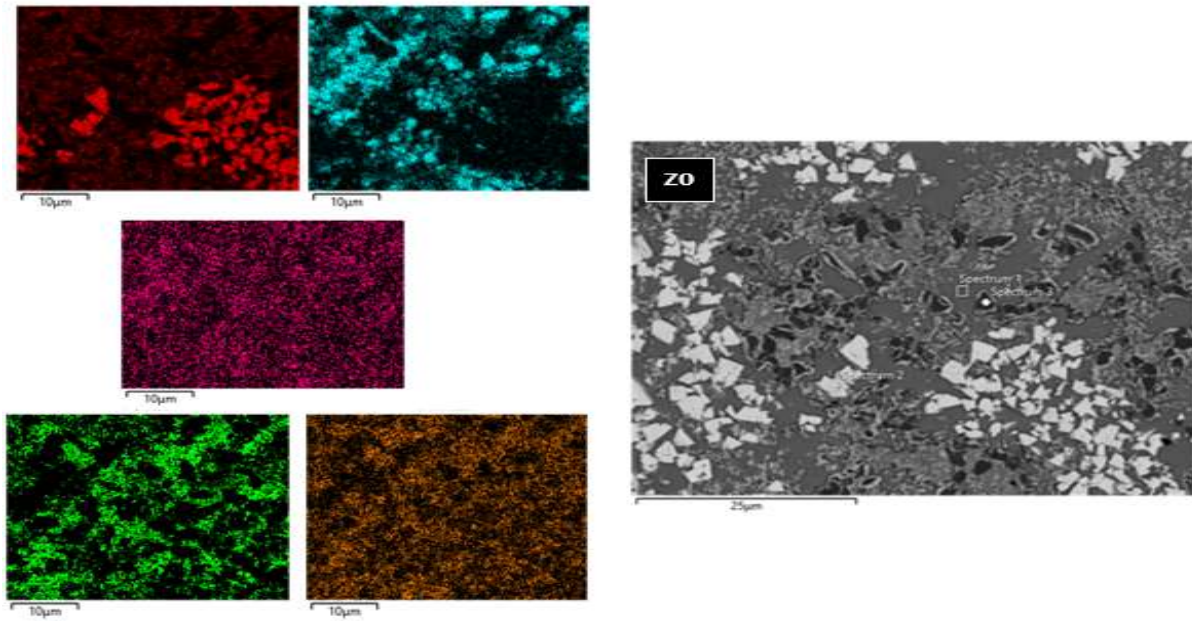
Figure 4.9: EDS analysis of composition Z0.

4.3.4 Category Y

In relation to the compositions within category Y, which represent an intermediate molar ratio of 1:3 between categories X and Z, the microstructure demonstrates the presence of only $(W, Ti)C$ phase dispersed within the matrix of Hadfield steel as shown in **Figure 4.10**.
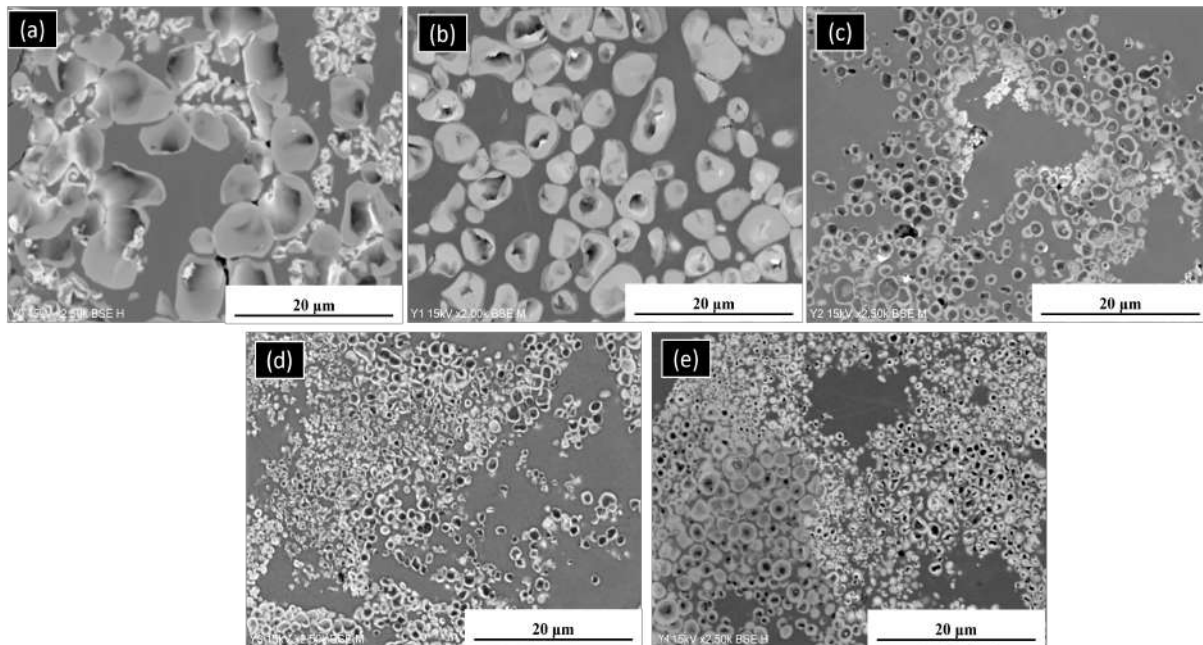
Figure 4.10: SEM images of category Y, (a): Y0, (b): Y1, (c): Y2 (d): Y3 and (e): Y4.

Compared to category X, the distribution and visibility of the $(W, Ti)C$ phase are more pronounced. Moreover, no WC particles were detected in this composition. Wang et al. [59] have highlighted that $(W, Ti)C$ exhibits superior overall performance compared to WC or TiC. This is attributed to the $(W, Ti)C$ phase combining desirable properties from hard ceramics such as

30

WC and *TiC*, making it particularly suitable for applications that require wear and abrasion resistances.

Figure 4.11 exhibits the X-ray mapping results, demonstrating the existence of $(W, Ti)C$ solid solution embedded within the matrix of Hadfield steel. The mapping provides a clear visualization of the dispersion patterns of different chemical elements. Notably, titanium exhibits higher concentration in the inner rim of the $(W, Ti)C$ solid solution, whereas both tungsten and titanium are observed in the outer rim. Meanwhile, chromium, manganese, and iron are predominantly present within the matrix of the material.
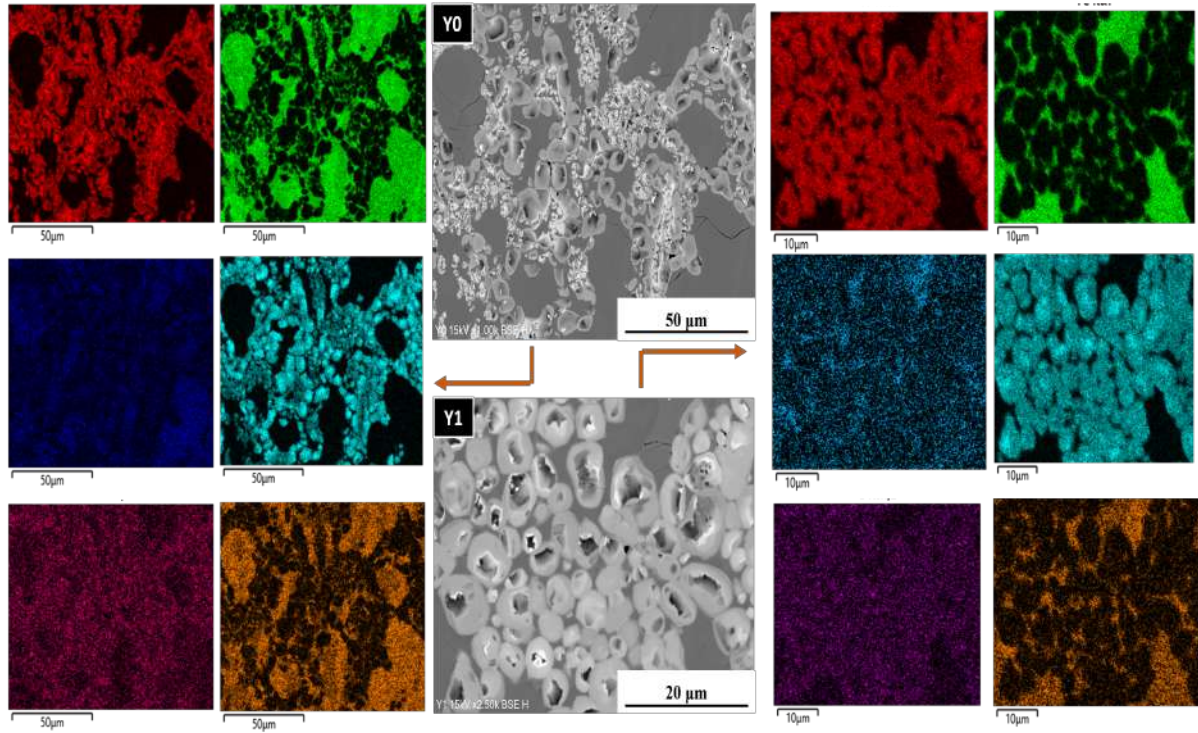
Figure 4.11: X-ray mapping results of compositions Y0 and Y1.

4.4 Particle size analysis

The particle size of the compositions was determined through manual measurement using the ImageJ software, with a minimum of 100 measurements taken. **Figure 4.12** displays the particle size distribution of each category. The binary carbide particles were compared in categories X and Y, while the tungsten carbides were compared in category Z, with the longest diagonal measurement utilized for the latter.

For instance, the particle size of binary carbides $(W, Ti)C$ in compositions X1, X2, and X3 were found to have decreased by 13 %, 27.6 %, and 46.8 %, respectively, in comparison to the composition X0 (**Figure 4.12-a**). Additionally, the inclusion of nickel in composition X4 exhibited a similar effect as iron. Furthermore, the particle size of WC in compositions Z1, Z3, and Z4 were measured to be 11.75 ± 3.36 μm, 10.4 ± 3.8 μm, and 5.47 ± 2.46 μm, respectively (**Figure 4.12-c**). Regarding category Y, the particle sizes of binary carbides (W,Ti)C were also measured in compositions Y0, Y1, Y2, Y3, and Y4. The respective measurements were found

to be 4.742 ± 1.17 µm, 3.822 ± 1.23 µm, 1.676 ± 0.39 µm, 1.145 ± 0.27 µm, and 1.09 ± 0.29 µm. Consequently, a decrease of 19.4 %, 64.6 %, 75.85 %, and 77 % was observed compared to the particle size in composition Y0 (**Figure 4.12-b**). Additionally, the binary carbide particles in category X were found to be larger than those in Y category.
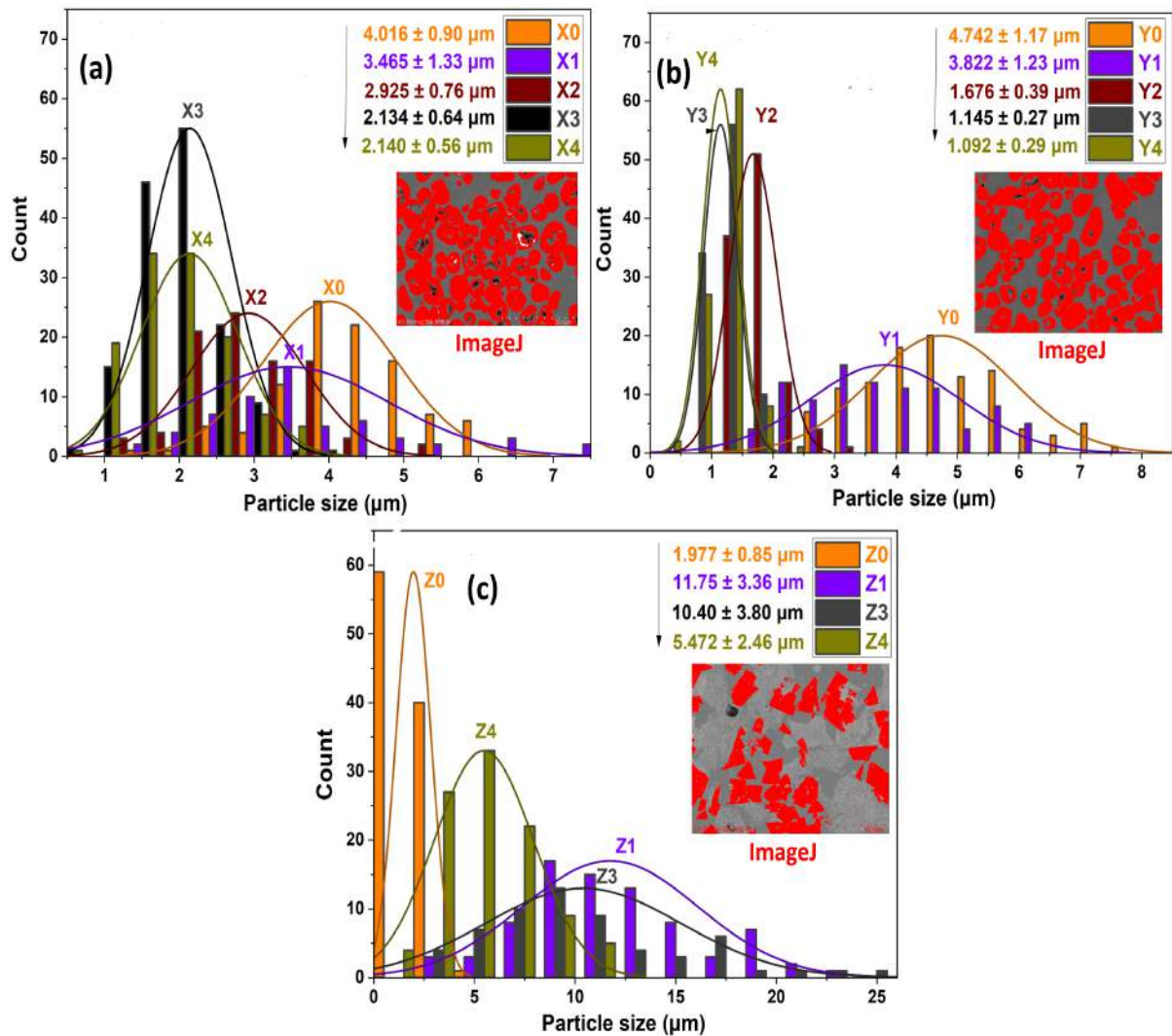
Figure 4.12: Particle size distribution, (a): category X, (b): category Y and (c): category Z.

It is possible to control carbide particle size by regulating the binder phase content. In the findings of Daoush et al. **[60]**, they stated that when the binder phase content is high, its distribution becomes uniform and prevents the coalescence of the carbide particles leading to the reduction of grain size and an overall decrease in carbide dimensions. Furthermore, Zhang et al. **[61]** reported that the addition of binder decreases the solubility of tungsten and limits the grain growth by solution–precipitation during sintering. Finer particle sizes provide a greater number of carbide particles dispersed in the matrix, resulting in increased resistance to wear. However, larger particle sizes can contribute to improved toughness. This is because larger particles act as crack arrestors, hindering crack propagation through their interaction with the crack front **[29]**.

4.5 Mechanical properties

4.5.1 Hardness of as cast Vs heat-treated quenched manganese steel

The average hardness values of the as cast and heat-treated specimens are 268 ± 24.92 HV and 212.41 ± 14.45 HV, respectively, as depicted in **Figure 4.13**. As the microscopy results have shown, the as-cast sample exhibits a higher chromium and manganese carbides content at the grain boundaries compared to the heat-treated sample, which correlates with the higher hardness observed in the as cast specimen [5]. These findings are in line with the results reported by Mousavi et Sabzi [62].
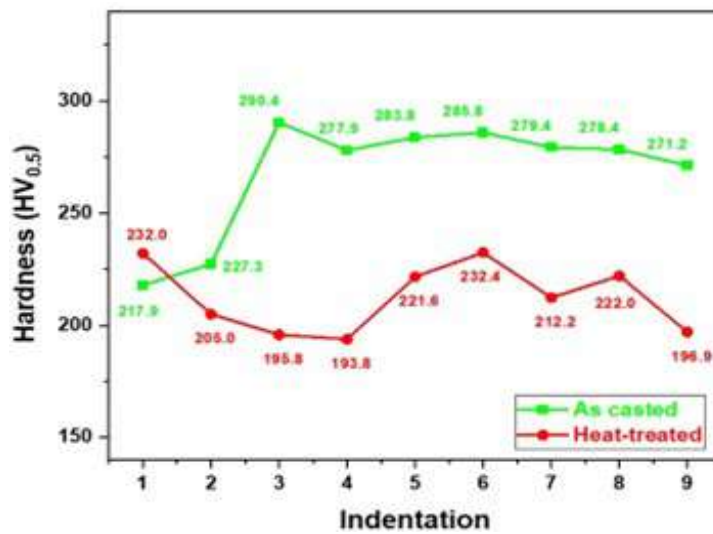
Figure 4.13: Hardness profile for as cast and heat-treated & quenched manganese steels.

4.5.2 Toughness of as cast Vs heat-treated and quenched steel

4.5.2.1 Fracture energy

Fracture energy measurements (Charpy test) were carried out on two samples of both as-cast and heat-treated and quenched steels as shown in **Figure 4.14**. The mean values can be found in **Table 4.1**.

Table 4.1: Fracture toughness measurements for as cast and heat-treated quenched manganese steel.

Sample	Nº	Impact toughness (J)	Main value (J)
H-treated & Quenched	1 2	69.81 82.73	76.27 ± 9.13
As cast	1 2	3.15 0.52	1.83 ± 1.86

As shown, the fracture toughness of the as-cast steel was determined to be 1.83 ± 1.86 J, while the heat-treated and quenched steel exhibited a toughness value of 76.27 ± 9.13 J. Consequently, the heat-treated and quenched sample demonstrates a higher ability to withstand greater amounts of energy or stress without fracturing compared to the as cast steel. This

disparity is likely attributed to the presence of carbides at the grain boundaries, leading to an increase in hardness. These findings align with the SEM and hardness results.
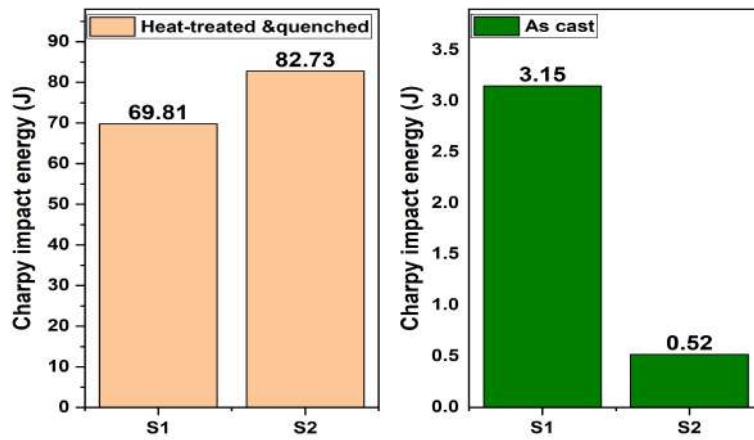
Figure 4.14: Fracture toughness for as cast and heat-treated and quenched manganese steel.

4.5.2.2 Fractured surfaces

The fracture surfaces of both samples were examined using SEM after conducting the Charpy test. SEM micrographs of these fracture surfaces are presented in **Figure 4.15**.
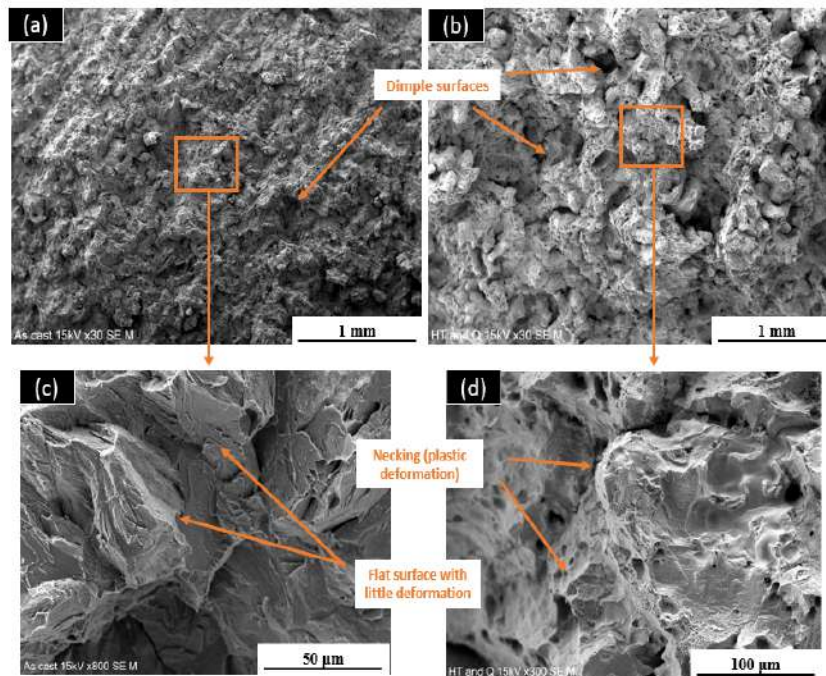
Figure 4.15: SEM micrographs of the fracture surfaces after Charpy test. (a): As cast, (b): Heat-treated & quenched, (c) and (d): Highlight areas showed in (a) and (b), respectively.

It is evident from the figure that heat-treated and quenched steel demonstrated a ductile fracture characterized by deeper dimples compared to the as-cast sample (**Figure 4.15-(a,b)**), indicating a higher level of ductility. These findings, coupled with the fracture energy results,

suggest that an increase in the amount of carbides in the as-cast steel reduces its ability to absorb shock and leads to embrittlement. Furthermore, the as-cast steel shows a lack of plastic deformation as can be seen in **Figure 4.15-c**, while the heat-treated and quenched steel displays evidence of necking or localized thinning because of its plastic deformation before fracture (**Figure 4.15-d**).

4.5.3   Hardness of Metal Matrix Composites (MMCs)

For each composition, a total of 18 indentations were performed across two lines to measure the hardness profile. Each line consisted of nine indentations: four in the matrix, four in the composite, and one at the interface. **Figure 4.16** provides a summary of the obtained results with corresponding to category X (**Figure 4.15-a**), Y (**Figure 4.16-c**) and Z (**Figure 4.16-c**), respectively. Generally, in all compositions, the hardness increases from the matrix, through the interface, and into the reinforced zone.
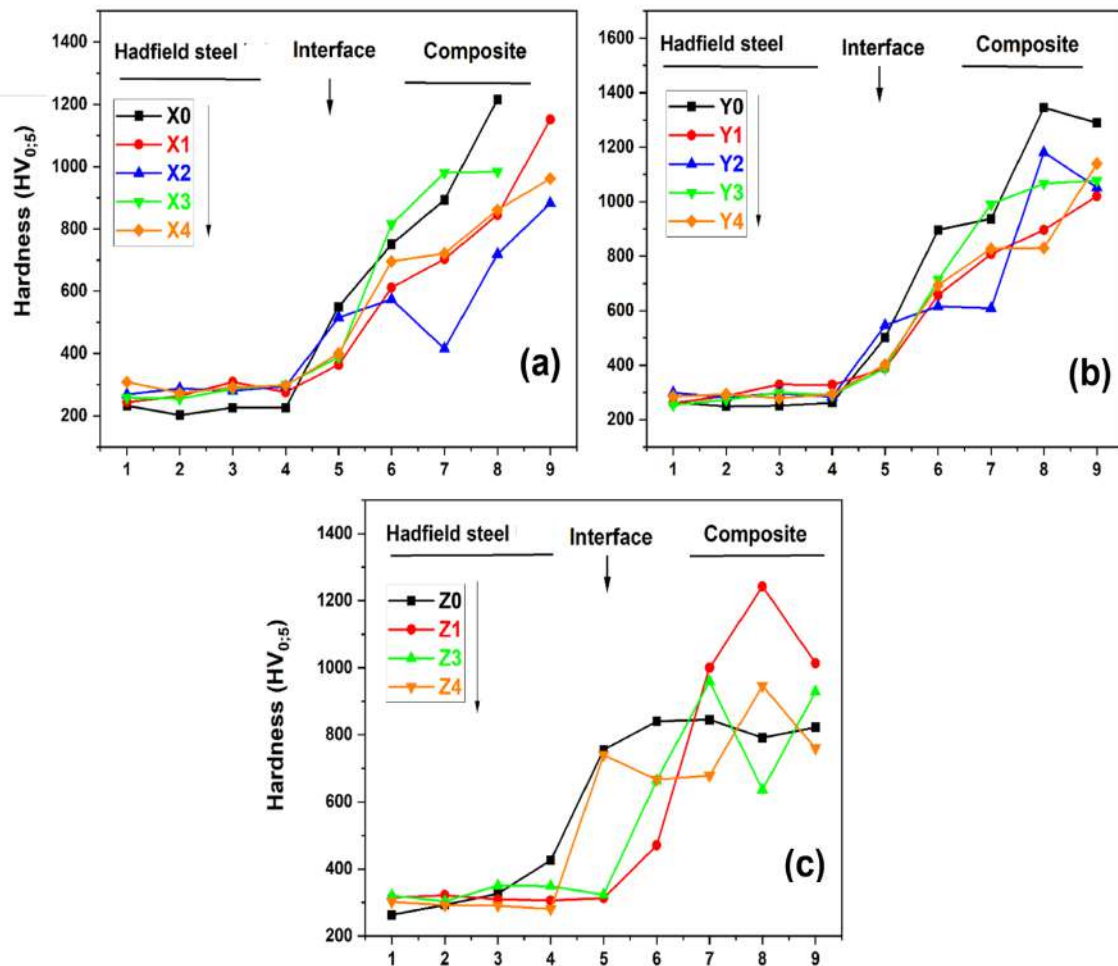
Figure 4.16: Hardness profiles of: (a): category X, (b): category Y, and (c): Category Z.

Based on the results depicted in **Figure 4.17** and **Table 4.2**, Hadfield steel exhibited an average hardness value of 300 HV across all compositions. The interface, where both carbides and Hadfield steel coexist, showed hardness values ranging from 320 HV to 640 HV. Additionally, the reinforced regions demonstrated a significant increase in hardness. For example, Z1 exhibited the highest hardness value of 1085.47 HV, while composition X2 displayed the low-

est hardness value of approximately 647.73 HV. Meanwhile, the interface displayed hardness values intermediate between those of the matrix and the composites. The increase in hardness is due to the presence of reinforcing particulate carbides $(Ti,W)C$ and WC, which act as obstacles to dislocation movement impeding plastic deformation in the matrix [28]. Furthermore, the difference in coefficient of thermal expansion (CTE) between Hadfield steel and carbide particulates can result in significant internal stresses and strains within the composite. These increased stress levels can enhance the hardness by rendering the material more resistant to deformation. According to reference [5], the (CTE) of Hadfield steel and WC are $1.7\sim2.5.10^{-5}K^{-1}$ and $5.5.10^{-5}K^{-1}$, respectively.

Table 4.2: Average hardness values of the matrix and MMCs.

ID	Hadfield steel	Interface	MMC
X0	221.49 ± 11.55	550.22 ± 11.53	859.49 ± 242.46
X1	272.81 ± 23.49	363.68 ± 13.71	827.97 ± 204.42
X2	282.92 ± 09.46	515.42 ± 22.98	647.73 ± 173.02
X3	275.00 ± 18.84	388.12 ± 24.56	693.51 ± 78.820
X4	292.43 ± 12.78	423.06 ± 10.89	809.88 ± 107.75
Y0	256.41 ± 06.63	501.00 ± 06.30	993.82 ± 201.84
Y1	301.02 ± 28.56	388.12 ± 04.54	845.37 ± 132.40
Y2	290.09 ± 08.09	515.42 ± 16.10	864.46 ± 255.94
Y3	279.30 ± 17.17	388.93 ± 12.45	847.28 ± 147.32
Y4	287.84 ± 06.36	402.97 ± 12.0	872.58 ± 163.52
Z0	294.20 ± 25.61	555.10 ± 21.01	810.75 ± 33.62
Z1	313.04 ± 05.93	312.96 ± 10.90	1085.47 ± 111.23
Z3	329.20 ± 17.94	323.07 ± 21.78	796.74 ± 147.22
Z4	291.24 ± 07.50	640.10 ± 43.10	758.07 ± 100.46
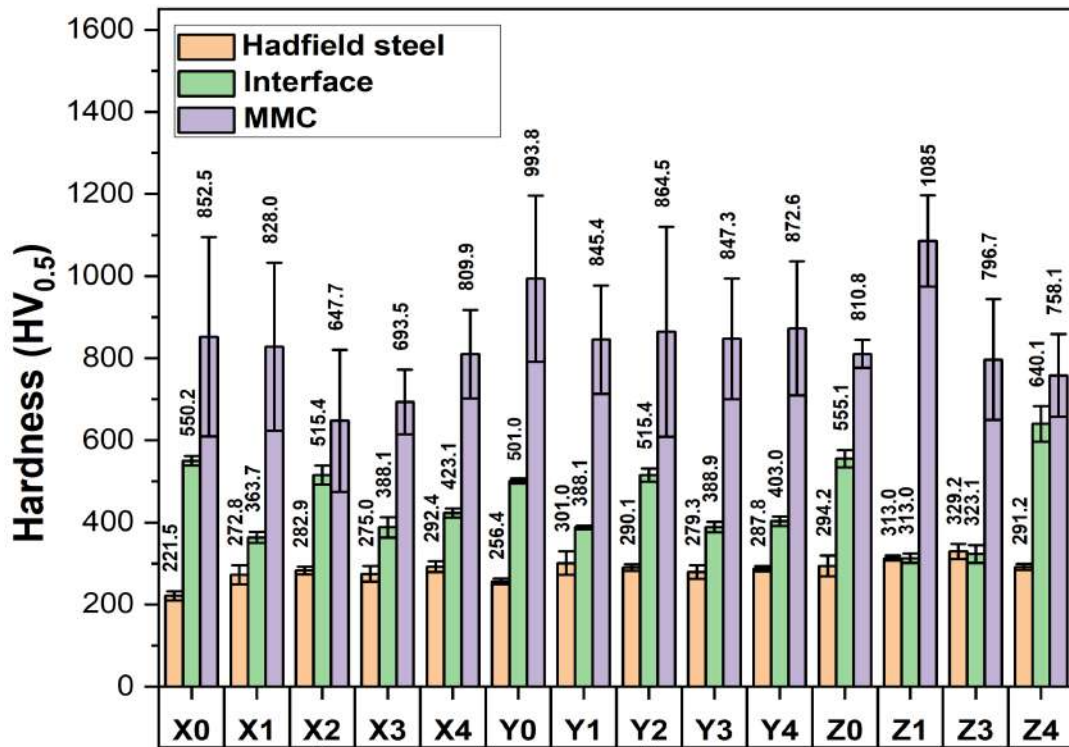
Figure 4.17: Average hardness values for matrix and composite profiles.

36

A slight decrease in hardness can be observed. The decrease in hardness may be attributed to the decrease in particle size of the carbides, as indicated in the particle size section, where the indentation contacts both the matrix and reinforced zone. According to reference [60], when the content of the metal binder is increased, it results in an increase in the thickness of the liquid phase surrounding the carbide phase. Consequently, the overall hardness of the composite decreases due to the contribution of the low hardness caused by the presence of the liquid phase binder. Moreover, He et al. [58] reported that the hardness decreases with increasing iron content due to its tenacity.

4.6 X-Ray Diffraction analysis

XRD analysis of manganese steel as depicted in **Figure 4.18**, indicate the presence of peaks corresponding to manganese carbides ($(Fe, Mn)_3C, Orthorhombic$) which are detected at 44.24° (121), 63.74° (301), and 83.24° (131). These carbides are caracteristics of manganese steel. These results align with the findings reported in the cited references **[5, 31, 62]**.
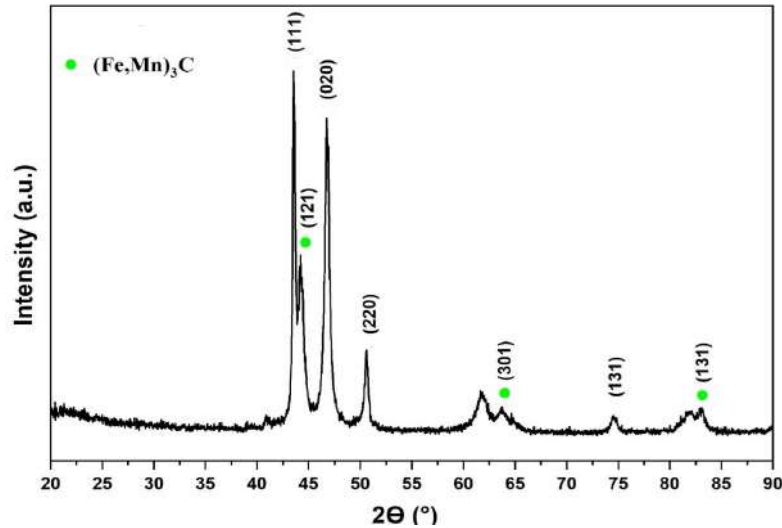
Figure 4.18: XRD patterns of manganese steel.

Regarding the XRD patterns of the composites, in categories X and Y, complete solid solution ($(W, Ti)C$) are obtained (**Figure 4.19-(a,b)**). However, in category Z, the WC phase coexists with a solid solution phase as shown in **Figure 4.19-c**. The peaks corresponding to binary carbides $(W, Ti)C$ (FCC) appear at 35.91° (111), 41.7° (020), 60.45° (022), and 72.35° (131), and 76.13° (222). Additionally, in category Z, peaks corresponding to WC (HPC) are observed at 31.49° (001), 35.63° (100), 48.25° (101), 64.01° (110), 65.8° (002), 75.1° (200), 77.23° (102), and 84.05° (201). However, no peaks corresponding to W_2C phase and η-phase (Eta-phase) are found in any of the samples **[30, 56]**. The XRD results obtained from these references are comparable **[37, 47, 59]**. Furthermore, these XRD findings align with the SEM micrographs and EDS analysis, providing confirmation of the presence of binary carbides and tungsten carbides phases.

According to references **[32, 47]**, the chemical formula of binary carbide solid solution is generally given by this formula $(W_x, Ti_{1-x})C_y$. Where x, is the mole fraction of W and the value of y is less than unity for phase stability reasons. The study of the chemical formula of
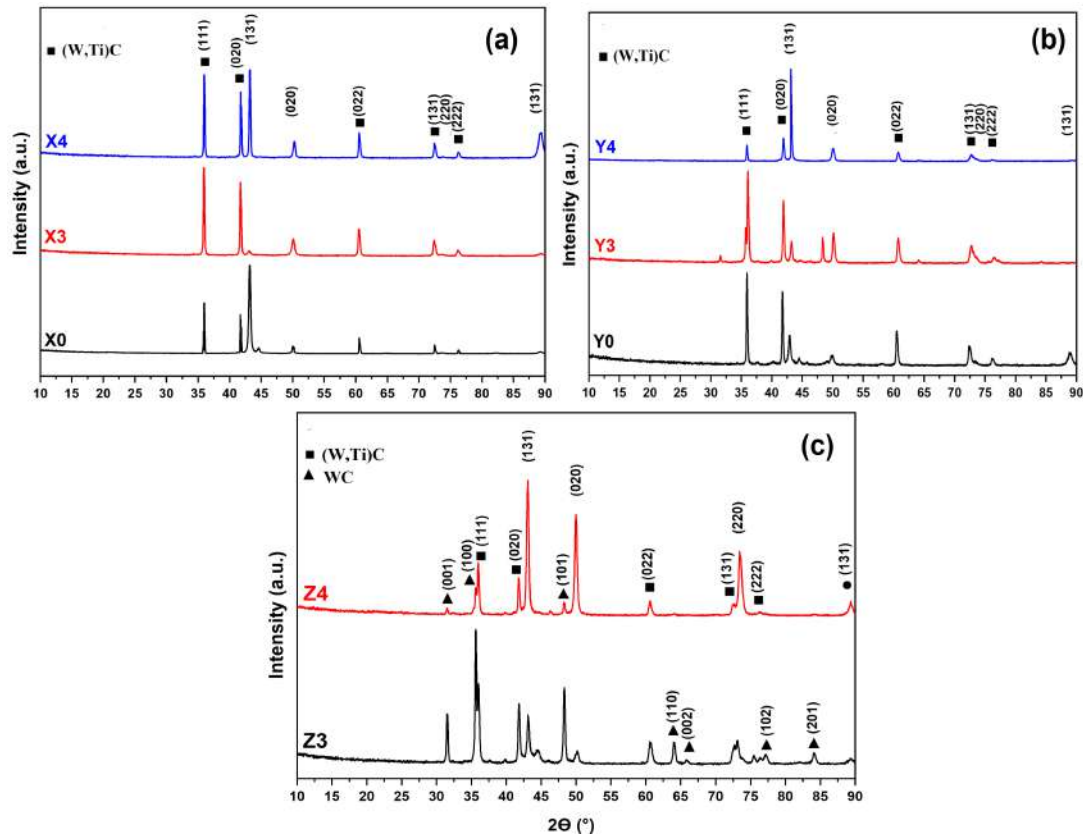
Figure 4.19: XRD patterns of MMCs, (a): category X, (b): category Y, and (c): category Z.

solid solution $(W,Ti)C$ has been also reported in the findings of Saidi et al [34]. For further investigation of this point, the lattice parameter of $(W,Ti)C$ versus the mole fraction of W has been compared. The results demonstrated that the lattice parameter of binary carbides decreases as the mole fraction of W is increased, this behavior of binary carbides adheres to Vegard's Law [33]. The shrinking lattice of $(Ti,W)C$ can be attributed to the diffusion of tungsten atoms into the lattice of $(Ti,W)C$. This is likely because the atomic radius of tungsten (1.3705 Å) is smaller than that of titanium (1.4318 Å) [61].

It is known that some alloy elements can form a solid solution with WC or $(W,Ti)C$, which may exhibit shifts in peak positions, broadening of peaks due to their incorporation into the lattice, and introduction of supplementary peaks [57]. However, the effect of these elements can barely be seen in few samples. Moreover, it is not possible to disscus the effect of binder since the amount of the matrix and carbides analyzed in each sample vary depending on the cut made on each sample. The same thing for the Rietveld method for phases quantification.

4.7 Wear resistance

4.7.1 Evaluation of volume loss

Due to the significant machining cost, only two compositions, specifically X3 and Y3, were subjected to testing. The detailed calculations and results of the wear testing can be found in **Table 4.3**. When comparing wear ratios, a lower value indicates superior wear resistance, meaning less weight or volume loss. In general, a wear ratio below 1 is considered favorable

as it suggests that the material experiences less wear in the abrasive environment. **Figure 4.20** below illustrates the volume loss of both the reference plates (Weldox) labeled 2&3 and the tested plates (X3 and Y3) labeled 1&4, in relation to the crushed abrasive's mass (1000 kg and 2000 kg). The density of Weldox plate is 7.72 $g.cm^{-3}$, while the densities of plates X3 and Y3 were calculated using the equations below, they were determined to be 7.53, 7.56 $g.cm^{-3}$, respectively. X is the volumetric fraction.

$$\rho_{composite} = \rho_{matrix} * X_{matrix} + \rho_{insert} * X_{insert} \quad \textbf{(9)}$$

Regarding the results:

- The volume loss increases with an increase in the crushed abrasive's mass for both, X3 and Y3 plates. This is evident since a higher mass of abrasive leads to more material being worn away, resulting in higher volume loss. Additionally, the relationship between the mass of the crushed abrasive and volume loss might be linear as it might be not linear [17].

- The volume loss of stationary jaw for both tested plates is higher than that of the movable one. The stationary and movable jaws of X3 composition presented differences of 56.27 % (SJ/MJ = 2.29) for 1000 kg and 57.69 % (SJ/MJ = 2.36) for 2000 kg. Similarly, the stationary and movable jaws of Y3 composition exhibited differences of 75.45 % (SJ/MJ = 4.07) for 1000 kg and 71.23 % (SJ/MJ = 3.48) for 2000 kg. This is likely related to the difference in wear micro-mechanisms along the stationary and movable jaws. According to Machado et al. [17], it was observed that the movable jaw exhibits a higher occurrence of micro-indentations, while the stationary jaw shows a prevalence of micro-cutting and micro-ploughing as the dominant micro-mechanisms. The micro-cutting involves the removal of materials through fracture and detachment, while the micro-indentation causes localized deformation and minimal material displacement. Lindqvist et al. [63] yielded similar findings, with the added observation that the wear rate on the stationary liner is 4–9 times greater than that on the moving liner.

- The volume loss experienced by Weldox plates was found to be greater compared to the X3 and Y3 plates. Upon crushing 2000 kg of abrasive particles, the volume loss for the Weldox plates was determined to be 9.16 cm^3 (MJ) and 49.66 cm^3 (SJ), surpassing the volume loss of the X3 plates which was 7.01 cm^3 (MJ) and 41.73 cm^3 (SJ) and the volume loss of Y3 plates which was 5.29 cm^3 (MJ) and 12.50 cm^3 (SJ). This difference can be attributed to the higher hardness of the Y3 and X3 plates, indicated by hardness values of 847.28 HV and 693.51 HV, respectively due to the presence of carbides, as opposed to the Weldox plates with a hardness value of 530 HV. Generally, materials with higher hardness exhibit better resistance against abrasives and result in a reduced wear rate. However, they are susceptible to breaking [3].

- The final wear ratios of X3 and Y3 plates were determined to be 0.190 and 0.516 for an abrasive mass of 1000 kg and 0.196 and 0.414 for an abrasive mass of 2000 kg. This indicates that X3 plates demonstrated superior resistance to wear despite its lower hardness. Generally, Y3 plates exhibit sufficient hardness to withstand abrasive forces than X3 plates. This outcome could potentially be attributed to the machining process as discussed in the following section.

Table 4.3: Final wear ratio calculation of composition Y3 and X3.

Plate		Y3		Reference (Weldox)		X3		Reference (Weldox)	
		MJ	SJ	MJ	SJ	MJ	SJ	MJ	SJ
Plate number		1	4	2	3	1	4	2	3
Initial mass (g)		3.5272	3.529	3.5736	3.582	3.6432	3.6056	3.5692	3.5814
Final mass (kg)	1000 kg	3.5000	3.4668	3.5364	3.3598	3.6362	3.5778	3.5404	3.3830
	2000 kg	3.4872	3.4344	3.5028	3.1984	3.6298	3.5602	3.5164	3.259
Mass loss (g)	1000 kg	27.2	62.2	37.2	222.2	7	27.8	28.8	198.4
	2000 kg	40.0	94.6	70.8	383.6	13.4	45.4	52.8	322.4
Volume loss (cm3)	1000 kg	3.60	8.22	4.82	28.76	0.91	3.69	3.82	25.68
	2000 kg	5.29	12.50	9.16	49.66	1.73	6.03	7.01	41.73
Final wear ratio	1000 kg	0.516				0.190			
	2000 kg	0.414				0.196			
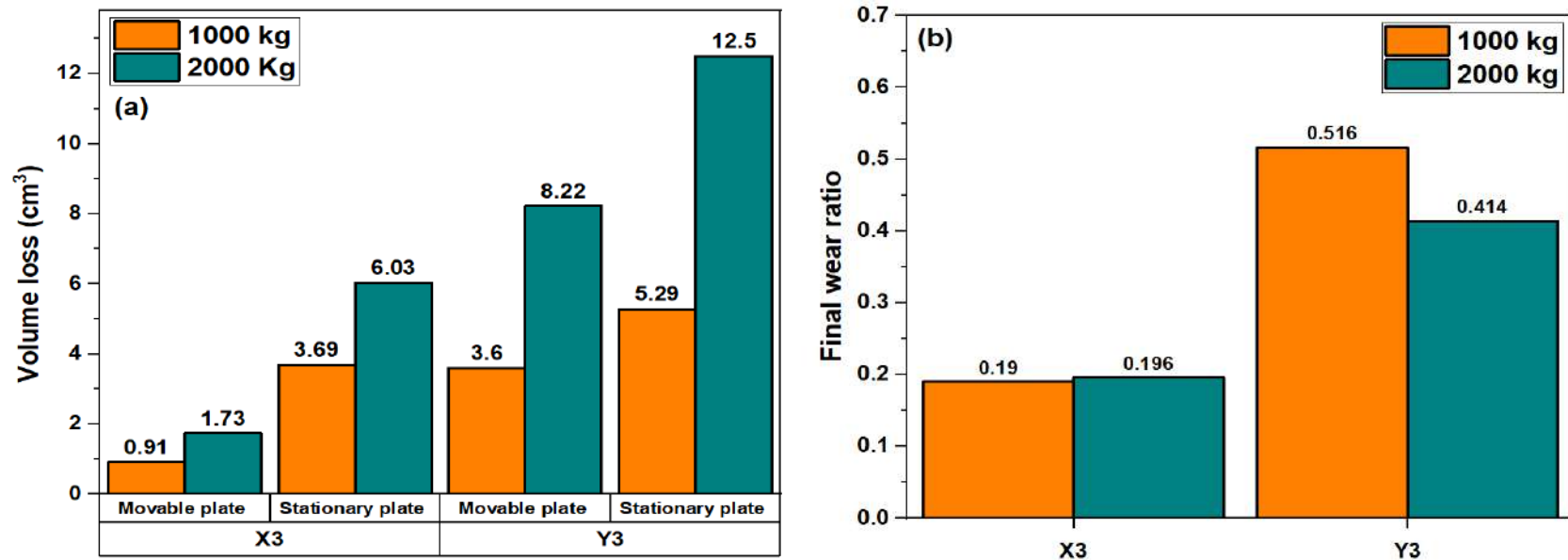
Figure 4.20: (a): Relationship between volume loss of tested plates and the crushed abrasive's mass. (b): calculated final wear ratios.

4.7.2 Worn surface

The SEM micrographs of the worn surface for both stationary and movable jaws are illustrated in **Figure 4.21-a** and **4.21-b**, respectively. They both exhibit a rough texture characterized by visible grooves and scratches, indicating an abrasive wear mechanism **[12, 17]**. This roughness is more pronounced in the stationary jaw due to a greater volume loss it has experienced. Moreover, the worn surface displays embedded abrasive fragments (darker areas in the images) and debris. X-ray mapping results in **Figure 4.21-c** reveal that these abrasive fragments primarily consist of oxygen (O), silicon (Si), aluminum (Al), calcium (Ca), sodium (Na), potassium (K), magnesium (Mg), and other chemical elements. This finding confirms the presence of abrasives like quartz, feldspar, mica, etc. Machado's research suggests that these embedded abrasive particles act as a secondary hard phase, protecting the surface and reducing the occurrence of extensive scratches **[17]**.
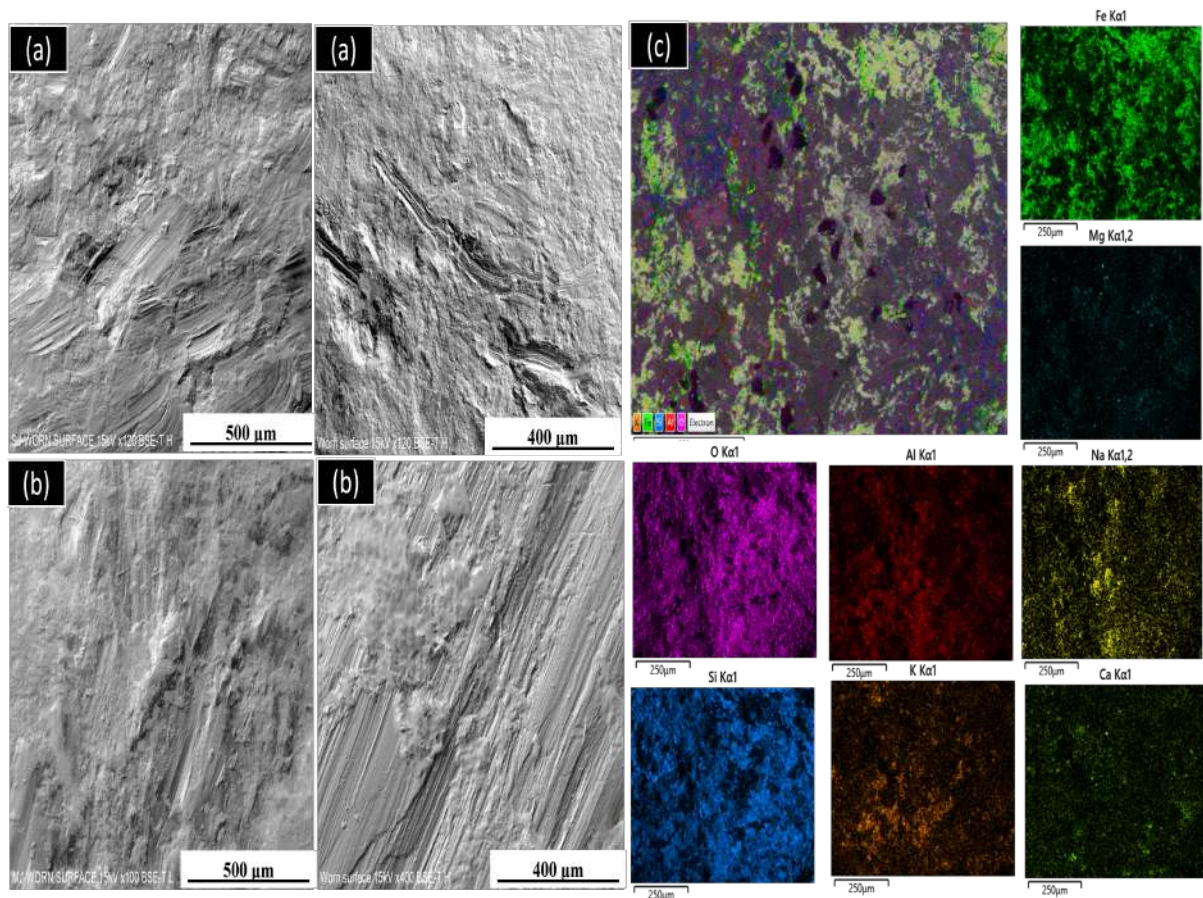
Figure 4.21: X-ray map SEM images of the worn surface. (a): SJ, and (b): MJ. (c): EDS analysis of the worn surface for the MJ.

4.7.3 Work hardening of manganese steel

Figure 4.22 shows the micro-hardness profile of manganese steel from the worn surface to the core for both stationary and movable jaws. The hardness profile exhibits a gradual decrease from the working surface towards the core for both stationary and movable jaws. Specifically, the micro-hardness near the working surface was measured at 346.16 HV for the stationary

jaw and 294.11 HV for the movable jaw. It has been reported by Olawale et al. [3] that the occurrence of high impacts leads to the formation of an extremely hard surface layer, which is 2-3 times harder than the alloy's core. This work-hardening behavior is a characteristic of manganese steel [63]. Hence, the combination of wear resistance (due to its hard surface) and impact strength (due to its ductile core) has established manganese steel as a vital material within the crushing industry.
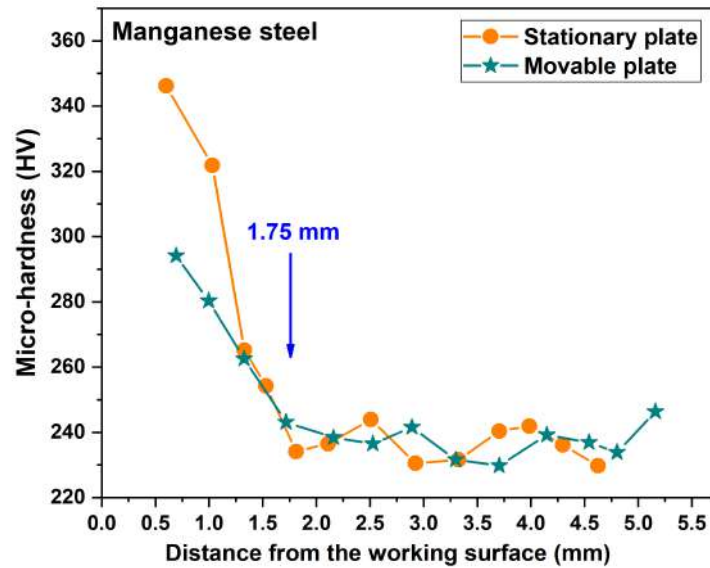
Figure 4.22: Micro-hardness profile from the working surface toward the core for both SJ and MJ plates of manganese steel.

Chapter 5

Conclusions

From the current research, the microstructure, and properties (hardness, wear resistance) of manganese steel reinforced with carbides have been investigated. Based on the findings, the following conclusions can be inferred.

- The metallic binders enhance the densification and reduce the grain size of carbides. However, there is no direct correlation between hardness values and metallic binder's content.
- The as cast manganese steel consists of manganese carbide phase $(Fe, Mn)_3C$ at the grain boundaries. Consequently, its hardness was found to be higher compared to heat treated and quenched steel. However, its fracture energy was lower.
- The microstructure of categories X and Y consists only of binary carbides $(W, Ti)C$. Meanwhile, the microstructure of categories Z consists of tungsten carbides (WC) along with binary carbides $(W, Ti)C$ as confirmed by EDS and XRD analysis.
- Despite the presence of certain flaws at the interface between the matrix and reinforcement, the samples exhibited robust and strong adhesion in these regions.
- In comparison to the hardness of the manganese steel matrix (212 HV), the MMCs exhibited a noteworthy hardness enhancement, ranging from 650 to 1100 HV.
- In terms of the wear test outcomes:
    - There were disparities in volume loss between the stationnary jay (SJ) and movable jaw (MJ), with the movable jaw (MJ) displaying greater resistance (lower volume loss) compared to the movable jaw.
    - The worn surface displays a coarse texture characterized by numerous visible grooves, scratches, and abrasive fragments, indicating the presence of abrasive wear.
    - The hardness profile demonstrates a gradual decrease from the worn surface towards the core for both the stationnary jay (SJ) and movable jaw (MJ), indicating the work hardening characteristic of manganese steel. Moreover, the hardening depth was determined to be 1.75 mm.
    - Composition X3 showed superior wear resistance compared to composition Y3. Besides, it has shown 42% decrease in the final wear ratio of manganese steel (0.33, this value was found by the previous students).

Chapter 6

Future work

The proposed next steps for this project are as follows:

- Conduct wear tests on a maximum number of samples.
- Establish a correlation between volume loss and the mass of crushed abrasives to estimate the wear rate and consequently the service life of jaw crushers.
- Conduct additional SEM imaging of the worn surface to gain deeper insights into the wear mechanisms.
- Enhance the mold setup to achieve improved results for the inserts, minimizing defects.
- Investigate the impact toughness of the samples and analyze the fracture surfaces to comprehend the fracture mechanism.

Chapter 7

Annexes

Annex I: main linear intercept method

• **Introduction:**

The mean linear intercept (m.l.i.) is probably the most widely used measurement of grain size, particularly in metallurgical research. The m.l.i. is measured from a linear traverse by counting the number of grain boundaries or grains, which intercept a linear traverse of length (L).

The m.l.i. is given by the following formula:

$$m.l.i. = d = \frac{L}{N}$$

Where, N is the number of grains intercepted.

• **Finding the number of intercepts (N):**

A random line of known length (L) is drawn, and then the number of intercepts (N) are counted according to the following rules. An example of calculating (N) is shown in figure below:

- If the test line goes through the grain, then N is equal to 1.
- If the test line terminates within the grain, then N is equal to 0.5.
- If the test line is tangential to a grain boundary, then N is equal to 0.5.
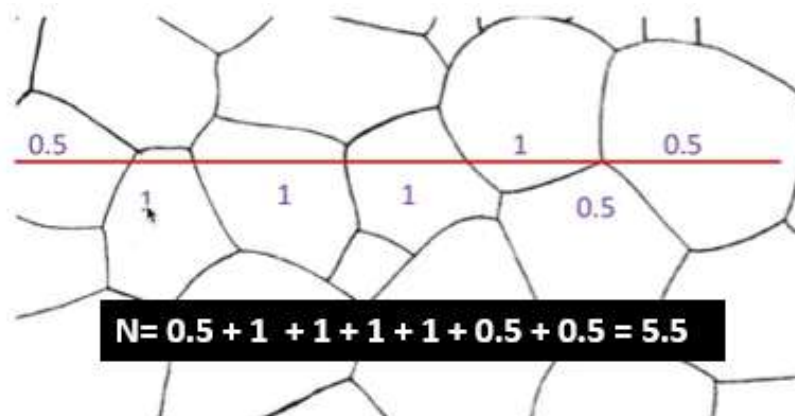
• **Assumptions according to test standards:**

- Equiaxed grains — Generally similar dimensions in every direction
- Grain boundaries are quite clear.
- Single phase structure.
- At least 50 grains in view.
- Clear magnification bar.

Bibliography

[1] S. Sandvik Group, "Rock processing," Sandvik Group. https://www.home.sandvik/en/.

[2] A. Mussatto, I. U. Ahad, R. T. Mousavian, Y. Delaure, and D. Brabazon, "Advanced production routes for metal matrix composites," Engineering Reports, vol. 3, no. 5, p. e12330, 2021, doi: 10.1002/eng2.12330.

[3] J. O. Olawale, S. A. Ibitoye, and M. D. Shittu, "Workhardening behaviour and microstructural analysis of failed austenitic manganese steel crusher jaws," Mat. Res., vol. 16, pp. 1274–1281, Dec. 2013, doi: 10.1590/S1516-14392013005000144.

[4] J. O. Olawale, S. A. Ibitoye, M. D. Shittu, and A. P. I. Popoola, "A Study of Premature Failure of Crusher Jaws," J Fail. Anal. and Preven., vol. 11, no. 6, pp. 705–709, Dec. 2011, doi: 10.1007/s11668-011-9511-7.

[5] A. K. Srivastava and K. Das, "In-situ Synthesis and Characterization of TiC-reinforced Hadfield Manganese Austenitic Steel Matrix Composite," ISIJ Int., vol. 49, no. 9, pp. 1372–1377, 2009, doi: 10.2355/isijinternational.49.1372.

[6] M. D. Hayat, H. Singh, Z. He, and P. Cao, "Titanium metal matrix composites: An overview," Composites Part A: Applied Science and Manufacturing, vol. 121, pp. 418–438, Jun. 2019, doi: 10.1016/j.compositesa.2019.04.005.

[7] M. Sabzi and M. Farzam, "Hadfield manganese austenitic steel: a review of manufacturing processes and properties," Mater. Res. Express, vol. 6, no. 10, p. 1065c2, Sep. 2019, doi: 10.1088/2053-1591/ab3ee3.

[8] S. Kumar, R. Singh, and M. S. J. Hashmi, "Metal matrix composite: a methodological review," Advances in Materials and Processing Technologies, vol. 6, no. 1, pp. 13–24, Jan. 2020, doi: 10.1080/2374068X.2019.1682296.

[9] L. L. Dong, M. Ahangarkani, W. G. Chen, and Y. S. Zhang, "Recent progress in development of tungsten-copper composites: Fabrication, modification and applications," International Journal of Refractory Metals and Hard Materials, vol. 75, pp. 30–42, Sep. 2018, doi: 10.1016/j.ijrmhm.2018.03.014.

[10] K. Shirvanimoghaddam et al., "Carbon fiber reinforced metal matrix composites: Fabrication processes and properties," Composites Part A: Applied Science and Manufacturing, vol. 92, pp. 70–96, Jan. 2017, doi: 10.1016/j.compositesa.2016.10.032. [

[11] A. Kumar, O. Vichare, K. Debnath, and M. Paswan, "Fabrication methods of metal matrix composites (MMCs)," Materials Today: Proceedings, vol. 46, pp. 6840–6846, Jan. 2021, doi: 10.1016/j.matpr.2021.04.432.

[12] S. Suresh and N. S. V. Moorthi, "Process Development in Stir Casting and Investigation on Microstructures and Wear Behavior of TiB2 on Al6061 MMC," Procedia Engineering, vol. 64, pp. 1183–1190, Jan. 2013, doi: 10.1016/j.proeng.2013.09.197.

[13] A. Ramanathan, P. K. Krishnan, and R. Muraliraja, "A review on the production of metal matrix composites through stir casting – Furnace design, properties, challenges, and research opportunities," Journal of Manufacturing Processes, vol. 42, pp. 213–245, Jun. 2019, doi: 10.1016/j.jmapro.2019.04.017.

[14] B. Venturelli, G. Tressia, and E. Albertin, "Effect of Manganese Content On The Wear Resistance And Impact Properties Of Hadfield Steel," Jul. 2022.

[15] E. R. Magdaluyo, M. S. Ausa, and R. J. Tinio, "Gouging Abrasion Resistance of Austenitic Manganese Steel with Varying Titanium," 2015.

[16] R. Zellagui, L. Hemmouche, H. Ait-Sadi, and A. Chelli, "Effect of Element Addition, Microstructure Characteristics, Mechanical Properties, Machining and Welding Processes of the Hadfield Austenitic Manganese Steel," Archives of Metallurgy and Materials, vol. 67, no. 3, p. 863, 2022.

[17] P. C. Machado, J. I. Pereira, and A. Sinatora, "Abrasion wear of austenitic manganese steels via jaw crusher test," Wear, vol. 476, p. 203726, Jul. 2021, doi: 10.1016/j.wear.2021.203726.

[18] M. Amirthalingam, "Microstructural Development during Welding of TRIP steels," 2010, Accessed: Apr. 13, 2023.

[19] A. García, Á. Varela, J. L. Mier, C. Camba, and F. Barbadillo, "Estudio tribológico de aceros austeníticos tipo Hadfield: influencia del manganeso en su respuesta frente al desgaste," Revista de Metalurgia, vol. 46, no. Extra, Art. no. Extra, Dec. 2010, doi: 10.3989/revmetalmadrid.04.1XIIPMS.

[20] W. D. C. Jr and D. G. Rethwisch, Fundamentals of Materials Science and Engineering: An Integrated Approach. John Wiley Sons, 2020.

[21] C. Su, G. Feng, J. Zhi, B. Zhao, and W. Wu, "The Effect of Rare Earth Cerium on Microstructure and Properties of Low Alloy Wear-Resistant Steel," Metals, vol. 12, no. 8, Art. no. 8, Aug. 2022, doi: 10.3390/met12081358.

[22] E. Brinksmeier, M. Garbrecht, and D. Meyer, "Cold surface hardening," CIRP Annals, vol. 57, no. 1, pp. 541–544, Jan. 2008, doi: 10.1016/j.cirp.2008.03.100.

[23] H. R. Jafarian, M. Sabzi, S. H. Mousavi Anijdan, A. R. Eivani, and N. Park, "The influence of austenitization temperature on microstructural developments, mechanical properties, fracture mode and wear mechanism of Hadfield high manganese steel," Journal of Materials Research and Technology, vol. 10, pp. 819–831, Jan. 2021, doi: 10.1016/j.jmrt.2020.12.003.

[24] S. Aribo, K. K. Alaneme, D. O. Folorunso, and F. O. Aramide, "Effect of Precipitation Hardening on Hardness and Microstructure of Austenitic Manganese Steel," JMMCE, vol. 09, no. 02, pp. 157–164, 2010, doi: 10.4236/jmmce.2010.92014.

[25] M. A. Valdes-Tabernero, C. Celada-Casero, I. Sabirov, A. Kumar, and R. H. Petrov, "The effect of heating rate and soaking time on microstructure of an advanced high strength steel," Materials Characterization, vol. 155, p. 109822, Sep. 2019, doi: 10.1016/j.matchar.2019.109822.

[26] J. P. Hilger and L. Bouirden, "New representation of the hardening processes of lead alloys by transformation-time-temperature (TTT) diagrams," Journal of Alloys and Compounds, vol. 236, no. 1, pp. 224–228, Apr. 1996, doi: 10.1016/0925-8388(95)02163-9.

[27] J. Moravec, M. Mičian, M. Málek, and M. Švec, "Determination of CCT Diagram by Dilatometry Analysis of High-Strength Low-Alloy S960MC Steel," Materials, vol. 15, no. 13, Art. no. 13, Jan. 2022, doi: 10.3390/ma15134637.

[28] A. K. Srivastava and K. Das, "Microstructure and abrasive wear study of (Ti,W)C-reinforced high-manganese austenitic steel matrix composite," Materials Letters, vol. 62, no. 24, pp. 3947–3950, Sep. 2008, doi: 10.1016/j.matlet.2008.05.049.

[29] J. García, V. Collado Ciprés, A. Blomqvist, and B. Kaplan, "Cemented carbide microstructures: a review," International Journal of Refractory Metals and Hard Materials, vol. 80, pp. 40–68, Apr. 2019, doi: 10.1016/j.ijrmhm.2018.12.004.

[30] A. S. Kurlov and A. I. Gusev, "Tungsten carbides and W-C phase diagram," Inorg Mater, vol. 42, no. 2, pp. 121–127, Feb. 2006, doi: 10.1134/S0020168506020051.

[31] S. Ashok Kumar and K. Das, "Corrosion Behaviour of TiC-Reinforced Hadfield Manganese Austenitic Steel Matrix In-Situ Composites," Open Journal of Metal, vol. 5, no. 2, Art. no. 2, Jun. 2015, doi: 10.4236/ojmetal.2015.52002.

[32] D. Bandyopadhyay, R. C. Sharma, and N. Chakraborti, "The Ti-Co-C system (titanium-cobalt-carbon)," JPE, vol. 21, no. 2, p. 179, Mar. 2000, doi: 10.1361/105497100770340246.

[33] M. J. Mas-Guindal, L. Contreras, X. Turrillas, G. B. M. Vaughan, Å. Kvick, and M. A. Rodríguez, "Self-propagating high-temperature synthesis of TiC–WC composite materials," Journal of Alloys and Compounds, vol. 419, no. 1, pp. 227–233, Aug. 2006, doi: 10.1016/j.jallcom.2005.08.079.

[34] A. Saidi, "Reaction synthesis of Fe–(W,Ti)C composites," Journal of Materials Processing Technology, vol. 89–90, pp. 141–144, May 1999, doi: 10.1016/S0924-0136(99)00049-7.

[35] K. H. Lee, S. I. Cha, B. K. Kim, and S. H. Hong, "Effect of WC/TiC grain size ratio on microstructure and mechanical properties of WC–TiC–Co cemented carbides," International Journal of Refractory Metals and Hard Materials, vol. 24, no. 1, pp. 109–114, Jan. 2006, doi: 10.1016/j.ijrmhm.2005.04.018.

[36] W. Acchar, C. R. F. da Camara, C. A. A. Cairo, and M. Filgueira, "Mechanical performance of alumina reinforced with NbC, TiC and WC," Mat. Res., vol. 15, pp. 821–824, Dec. 2012, doi: 10.1590/S1516-14392012005000120.

[37] Y. Choi and S.-W. Rhee, "Effect of iron and cobalt addition on TiC combustion synthesis," Journal of Materials Research, vol. 8, no. 12, pp. 3202–3209, Dec. 1993, doi: 10.1557/JMR.1993.3202.

[38] E. O. Correa, J. N. Santos, and A. N. Klein, "Microstructure and mechanical properties of WC Ni–Si based cemented carbides developed by powder metallurgy," International Journal of Refractory Metals and Hard Materials, vol. 28, no. 5, pp. 572–575, Sep. 2010, doi: 10.1016/j.ijrmhm.2010.04.003.

[39] G. Cliche and S. Dallaire, "Synthesis of TiC and (Ti, W)C in solvent metals," Materials Science and Engineering: A, vol. 148, no. 2, pp. 319–328, Dec. 1991, doi: 10.1016/0921-5093(91)90834-A.

[40] C. M. Fernandes, V. Popovich, M. Matos, A. M. R. Senos, and M. T. Vieira, "Carbide phases formed in WC–M (M=Fe/Ni/Cr) systems," Ceramics International, vol. 35, no. 1, pp. 369–372, Jan. 2009, doi: 10.1016/j.ceramint.2007.11.001.

[41] J. Li, Z. Zheng, and Z. Zhang, "Self-propagating high-temperature synthesis of (W, Ti) C powders," J Cent. South Univ. Technol., vol. 6, no. 2, pp. 124–126, Nov. 1999, doi: 10.1007/s11771-999-0013-7.

[42] J. Subrahmanyam and M. Vijayakumar, "Self-propagating high-temperature synthesis," J Mater Sci, vol. 27, no. 23, pp. 6249–6273, Dec. 1992, doi: 10.1007/BF00576271.

[43] P. Mossino, "Some aspects in self-propagating high-temperature synthesis," Ceramics International, vol. 30, no. 3, pp. 311–332, Jan. 2004, doi: 10.1016/S0272-8842(03)00119-6.

[44] E. A. Levashov, A. S. Mukasyan, A. S. Rogachev, and D. V. Shtansky, "Self-propagating high-temperature synthesis of advanced materials and coatings," International Materials Reviews, vol. 62, no. 4, pp. 203–239, May 2017, doi: 10.1080/09506608.2016.1243291.

[45] Z. Y. Fu, H. Wang, W. M. Wang, and R. Z. Yuan, "Composites fabricated by self-propagating high-temperature synthesis," Journal of Materials Processing Technology, vol. 137, no. 1, pp. 30–34, Jun. 2003, doi: 10.1016/S0924-0136(02)01061-0.

[46] Katgerman, L. and Martinez Pacheco, M., "Self-sustained high-temperature reactions," 2007. Accessed: Apr. 13, 2023. [Online]. Available: http://resolver.tudelft.nl/uuid:72d4ec8b-997e-49e5-8cf3-53a2fe6a038d

[47] G. Jiang, W. Li, and H. Zhuang, "Synthesis of tungsten carbide–nickel composites by the field-activated combustion method," Materials Science and Engineering: A, vol. 354, no. 1, pp. 351–357, Aug. 2003, doi: 10.1016/S0921-5093(03)00038-8.

[48] J. Jung and S. Kang, "Sintered (Ti,W)C carbides," Scripta Materialia, vol. 56, no. 7, pp. 561–564, Apr. 2007, doi: 10.1016/j.scriptamat.2006.12.026.

[49] M. Ferran Alvarez, "Microstructure and Mechanical Investigation of Reinforced Hadfield Steel," Luleå University Of Technology, Division of Materials Science Experimental Physics, Jun. 2022.

[50] G. Jordi Giménez, "Correlation between mechanical and wear properties of reinforced Hadfield steel.," Luleå University Of Technology, Department of Engineering Sciences and Mathematics, 2022.

[51] F. Asier Soria, "Effect of the compaction pressure on the mechanical properties and microstructure of reinforced Hadfield steel.," Luleå University Of Technology, Division of Materials Science Experimental Physics, Jun. 2022.

[52] G. Roger Ribas, "Tribological Properties of Hadfield Steel Composite.," Luleå University Of Technology, Division of Materials Science Experimental Physics, Jun. 2022.

[53] K. Hema and B. Manideep, "Wear Performance Investigation of Metal Matrix Composites (MMCs)," Lund University, Division Of Production and Materials Engineering, Jun. 2021.

[54] A. Terlikbaeva et al., "Synthesis and Sintering of Tungsten and Titanium Carbide: A Parametric Study," Metals, vol. 12, no. 12, Art. no. 12, Dec. 2022, doi: 10.3390/met12122144.

[55] Y. Pan et al., "Effects of metal binder content and carbide grain size on the microstructure and properties of SPS manufactured WC–Fe composites," Journal of Alloys and Compounds, vol. 784, pp. 519–526, May 2019, doi: 10.1016/j.jallcom.2019.01.057.

[56] N. Wu et al., "Effects of WC content on core/rim phases and microstructure of TiB2-TiC-WC-(Co-Ni) cermets," Materials Today Communications, vol. 25, p. 101311, Dec. 2020, doi: 10.1016/j.mtcomm.2020.101311.

[57] J. Kübarsepp and K. Juhani, "Cermets with Fe-alloy binder: A review," International Journal of Refractory Metals and Hard Materials, vol. 92, p. 105290, Nov. 2020, doi: 10.1016/j.ijrmhm.2020.105290.

[58] M. He, J. Wang, R. He, H. Yang, and J. Ruan, "Effect of cobalt content on the microstructure and mechanical properties of coarse grained WC-Co cemented carbides fabricated from chemically coated composite powder," Journal of Alloys and Compounds, vol. 766, pp. 556–563, Oct. 2018, doi: 10.1016/j.jallcom.2018.06.366.

[59] J. Wang et al., "Mechanical property and cutting performance of (W,Ti)C based ceramic composites with the addition of nano-sized CaF2," International Journal of Refractory Metals and Hard Materials, vol. 99, p. 105607, Sep. 2021, doi: 10.1016/j.ijrmhm.2021.105607.

[60] W. M. Daoush, K. H. Lee, H. S. Park, and S. H. Hong, "Effect of liquid phase composition on the microstructure and properties of (W,Ti)C cemented carbide cutting tools," International Journal of Refractory Metals and Hard Materials, vol. 27, no. 1, pp. 83–89, Jan. 2009, doi: 10.1016/j.ijrmhm.2008.04.003.

[61] G. Zhang, W. Xiong, Q. Yang, Z. Yao, S. Chen, and X. Chen, "Effect of Mo addition on microstructure and mechanical properties of (Ti,W)C solid solution based cermets," International Journal of Refractory Metals and Hard Materials, vol. 43, pp. 77–82, Mar. 2014, doi: 10.1016/j.ijrmhm.2013.11.004.

[62] S. H. Mousavi Anijdan and M. Sabzi, "The Effect of Heat Treatment Process Parameters on Mechanical Properties, Precipitation, Fatigue Life, and Fracture Mode of an Austenitic Mn Hadfield Steel," J. of Materi Eng and Perform, vol. 27, no. 10, pp. 5246–5253, Oct. 2018, doi: 10.1007/s11665-018-3625-y.

[63] M. Lindqvist and C. M. Evertsson, "Liner wear in jaw crushers," Minerals Engineering, vol. 16, no. 1, pp. 1–12, Jan. 2003, doi: 10.1016/S0892-6875(02)00179-6.